THESIS FOR THE DEGREE OF DOCTOR OF PHILOSOPHY

Mechanistic Approach to Corrosion of Zirconium by Water
- *A First Principle Study*

MIKAELA LINDGREN

Department of Chemistry and Chemical Engineering
CHALMERS UNIVERSITY OF TECHNOLOGY
Göteborg, Sweden 2018

Mechanistic Approach to Corrosion of Zirconium by Water
- *A First Principle Study*
MIKAELA LINDGREN

ISBN 978-91-7597-555-9
Doktorsavhandlingar vid Chalmers tekniska högskola
Ny serie nr 4236
ISSN 0346-718X

Department of Chemistry and Chemical Engineering
CHALMERS UNIVERSITY OF TECHNOLOGY
SE-412 96 Göteborg
Sweden
Telephone +46 (0)31 772 1000

Cover:
Left: An electron orbital (green) with the center of the H-part in a Fe associated three-center hydride ion. Oxygen is represented as red, zirconium as light blue, hydrogen as white and iron as purple. *Middle:* Schematic drawing of the oxidation process where the barrier oxide consists of a duplex oxide with both tetragonal and monoclinic zirconia. *Right:* Highest occupied Kohn-Sham state for pore structure with one hydrogen atom inserted into the pore. Notice the localised nature of the orbitals associated with the hydrogen atom.

Printed by Reproservice
Göteborg, Sweden 2018

Mechanistic Approach to Corrosion of Zirconium by Water - *A First Principle Study*

MIKAELA LINDGREN
Department of Chemistry and Chemical Engineering, Chalmers University of Technology

Abstract
Zirconium and zirconium oxides are of major technological importance. There are broad applications for these materials, from fuel cell electrolyte to semiconductors and in hip-implants. In nuclear power plants, zirconium alloys are widely used as cladding material to contain the fission fuel in the reactor cores. A limiting factor for fuel longevity is the corrosion properties of the zirconium alloys. The main corrodent in the reactor core is water. The oxidation process of zirconium alloys with water should ideally be accompanied by molecular hydrogen release into the surrounding, but a significant amount of hydrogen is absorbed into the alloy. This process is called hydrogen pick-up, and is along with the oxidation rate decisive to the durability of the cladding. Mechanisms controlling hydrogen pick-up are to a large extent unknown.

In this study density functional theory, DFT, is used to gain insights into the mechanism for water induced corrosion of zirconium. The purpose is to build understanding by deconstructing the corrosion phenomenon into computationally accessible and at the same time experimentally relevant quantum chemical modules. Anode and cathode reactions of the system are explored and a charge dependent oxygen vacancy transport through zirconia is identified. A detailed mechanism for electro-catalytic hydrogen evolution is articulated. It comprises formation of a transition metal associated hydride ion that recombines with a proton to form molecular hydrogen. The concentration dependence of the anode potential on absorbed oxygen in the alloy is examined along with the impact of co-absorption of oxygen and hydrogen in the α-Zr matrix. Two channels are taken to jointly constitute the oxidation process: one according to classical oxidation theory involving hydrogen evolution and the second reflected by inwards transport of protons causing hydrogen pick-up. Wagner theory and Tedmon kinetics are modified to include effects of oxide scale charging by augmenting the activation energy for diffusion of charged oxygen vacancies to also include the actual charging upon formation. Hydrogen assisted build-up of nano-porosity is also addressed.

Keywords: hydrogen pick-up, DFT, zirconium, corrosion, oxygen vacancy

Preface

The research work in this thesis was carried out at the Energy and Material Division at the Department of Chemistry and Chemical Engineering, Chalmers University of Technology, Göteborg, Sweden during the period January 2012 to April 2017, under the supervision of Professor Itai Panas. The work was as part of the MUZIC-2 (Mechanistic Understand of Zirconium Corrosion) collaboration and was funded by Westinghouse Electric Sweden, Electric Power Research Institute (EPRI), the Swedish Research Council, Sandvik Materials Technology, and Vattenfall.

List of publications

This thesis is based on the work contained in the following publications, referred to by Roman numerals in the text.

I. M. Lindgren, G. Sundell, I. Panas, L. Hallstadius, M. Thuvander, H.-O. Andren, "Toward a Comprehensive Mechanistic Understanding of Hydrogen Uptake in Zirconium Alloys by Combining Atom Probe Analysis With Electronic Structure Calculations", *ASTM Special Technical Publication*, **STP 1543**, 515-539 (2015).

II. M. Lindgren and I. Panas, "Impact of Additives on Zirconium Oxidation by Water: Mechanistic Insights from First Principles", *RSC Advances* **3**, 21613-21619 (2013).

III. M. Lindgren and I. Panas, "Confinement Dependence of Electro-Catalysts for Hydrogen Evolution from Water Splitting", *Beilstein Journal of Nanotechnology* **5**, 195-201 (2014).

IV. M. Lindgren and I. Panas, "On the Fate of Hydrogen during Zirconium Oxidation by Water: Effect of oxygen dissolution in α-Zr", *RSC Advances* **4**, 11050-11058 (2014).

V. M. Lindgren, C. Geers and I. Panas, "Oxidation of Zr Alloys by Water - Theory from First Principles", To be submitted

VI. M. Lindgren and I. Panas, "Oxygen Vacancy Formation, Mobility and Hydrogen Pick-up during Oxidation of Zirconium by Water", *Oxidation of Metals* **87**, 355-365 (2017).

VII. M. Lindgren, C. Geers and I. Panas, "Possible Origin and Roles of Nanoporosity in ZrO_2 Scales for Hydrogen Pick-up in Zr Alloys", *Journal of Nuclear Materials* **492**, 22-31 (2017).

Statement of author's contribution

I am first author of all papers in the thesis and I preformed all calculations. My supervisor and I did the analysis of results and the writing of the papers in collaboration. Paper I is an exception, I have not contributed to the atom probe tomography study or analysis of those results, nor to the writing of the sections *Experimental considerations* and *Experimental details*.

Acknowledgements

First of all, I would like to thank my supervisor Itai Panas for your support, discussions, and for always having time for me.

Special thanks to my examiner Jan-Erik Svensson. My director of study Hanna Härelind, as well as my former director of study Sten Eriksson, are both acknowledged for their support, guidence, and inspiration.

Moreover, I would like to thank all participants in the MUZIC-2 collaboration, your comments and question on the biannual meetings have been very valuable. All post and present members in the Swedish project "Mechanisms of hydrogen uptake in zirconium alloys" are gratefully acknowledged for your input, questions and industry perspective on my research that have been invaluable. Especially, thank you to Lars Hallstadius from Westinghouse, Gustav Sundell, Christine Geers, Hans-Olof Andrén and Mattias Thuvander from Chalmers for your collaboration with papers and your fruitful scientific discussions.

Westinghouse Electric Sweden, EPRI, the Swedish Research Council, Sandvik Materials Technology, and Vattenfall are gratefully acknowledged for financial support.

Finally, I would also like to thank my family, especially mamma, pappa and Martin, for your support and presence. Oskar, thank you for your endless love, support and encouragement. Isak and Vera, thank you for being you.

Göteborg, August 2018
Mikaela Lindgren

Contents

Chapter 1

Introduction

1.1 Background

Humanity faces a complex energy challenge that must be resolved during this century. Energy demand globally is increasing due to growing world population and improved standards living worldwide. At the same time, there is an increasing concern for the climate where greenhouse gase emissions need to be reduced [1, 2]. In anticipation of reliable and cost efficient technologies for large scale environmentally friendly and sustainable energy sources, manycountries turn to nuclear power which is relatively cheap and fulfill the requirement concerning low emission of greenhouse gases [3, 4]. However, there are significant drawbacks with nuclear power, that include how mine the uranium ore, how handle the radioactive waste and how to ensure safety during power production. Climate change mitigation is possible without the use of nuclear power (e.g. [5, 6]), but it may become more difficult and more costly to achieve the required mile stones if we exclude nuclear power from the energy system [7–10].

For the last 60 years, zirconium alloys have been the dominating cladding material for the purpose of containing the nuclear fuel in light water reactors [11, 12]. Zirconium alloys are also used in other core components. Extensive knowledge about zirconium alloys in reactor conditions have been acquired since the 1950's, but this is still an active research field and there are still complex phenomena that need to be understood in order to achieve increased efficiency. The trend the last decades has been towards increased fuel burnup by letting the fuel stay in the reactor for a longer time. As a consequence, issues related to the corrosion

properties of the zirconium cladding have increased in importance.

Ideally, the oxidation process of zirconium alloys with water should be accompanied by molecular hydrogen release into the surrounding. Yet, it was found very early [13, 14] that a significant amount of hydrogen was absorbed into the alloy causing embrittlement as well as deformation of the fuel rods, both being decisive to the longevity of the fuel. The main goal of research into zirconium alloys corrosion is to achieve lower oxidation rates and at the same time ensure that the fraction of hydrogen that is picked up by the alloy stays low.

In order to make progress in the quest for understanding as to the mechanisms that control the hydrogen pick-up fraction, a variety of different research techniques and approaches, both experimental and theoretical, are being used. In this spirit, the MUZIC-2 research program is conducted as a collaborative project between industry and academic partners. My PhD project is part of this collaboration. MUZIC stands for *Mechanistic Understanding of Zirconium Corrosion*. Following organizations are members of the MUZIC-2 consortium:

AMEC Foster Wheeler (now Wood)
Chalmers University of Technology
Électricité the France (EDF)
Electric Power Research Institute (EPRI)
Imperial College London
National Nuclear Laboratory (U.K.)
Paul Scherrer Institute
Pennsylvania State University
Rolls-Royce
Sandvik Materials Technology
Studsvik Nuclear
University of Manchester
University of Oxford
Vattenfall
Westinghouse Electric Company

1.2 Aim of this study

The aim of this study is to increase the knowledge about mechanisms that govern hydrogen uptake in zirconium alloys. The work is focused on atomistic modelling using Density Functional Theory, DFT [15, 16]. Mechanistic insights re-

garding water induced corrosion of zirconium alloys with particular emphasis on the dual fate of hydrogen is sought. Although converged numbers are provided, the objective is not the numbers as such but rather to gain conceptual insight by means of first-principles calculations. And rather than the final answer, this studysupports the development of an emerging comprehensive internally consistent understanding, to serve conceptual tool for the experiment. As one of two theoretical project in the MUZIC-2 collaboration, an important purpose of the present study is to challenge the experimental partners and offer interpretations to observations. This work is relevant to corrosion of zirconium alloys by water under autoclave conditions, e.g. no effects of irradiation are explicitly included in the modelling. Indeed, the MUZIC-2 consortium as a whole made extensive use of the autoclave experiments to mimic in reactor conditions.

Chapter 2

Zirconium in the nuclear industry

Nuclear power is the most efficient energy source available today. Zirconium components are used in nuclear reactor cores and corrosion properties of these components are of major importance for the time the nuclear fuel can be used in the reactor. Thus, properties of the zirconium components influence how efficient the nuclear fuel can be used and in the long run the efficiency of the nuclear power plants.

2.1 Nuclear reactors

Electricity produced by nuclear power plants is generated by steam turbines that are connected to electric generators. There are different types of reactors and the most commonly used today are light water reactors (LWR). There are two types of LWR: boiling water reactor (BWR) and pressurized water reactor (PWR). In a LWR, it is light water, H_2O, that acts as coolant of the core and moderator to decrease the energy of the neutrons. This is in contrast to e.g. in CANDU reactors where heavy water, D_2O, is used as coolant and moderator. The main difference between BWR and PWR plants is where the steam to the steam turbines is produced. In a BWR plant, steam is generated in the reactor core and in a PWR plant is steam produced in a second water circle heated by the water from the reactor core, see Fig. 2.1. The heat that produce the steam is caused by the radiation generated by fission reactions in the reactor core. In the fission reaction a ^{235}U-nucleus is hit by a thermal neutron and a ^{236}U-nucleus is formed. The ^{236}U isotope is unstable and decomposes into fission products, fast neutrons and γ-radiation [17], see illustration in Fig. 2.2. These fast neutrons have an

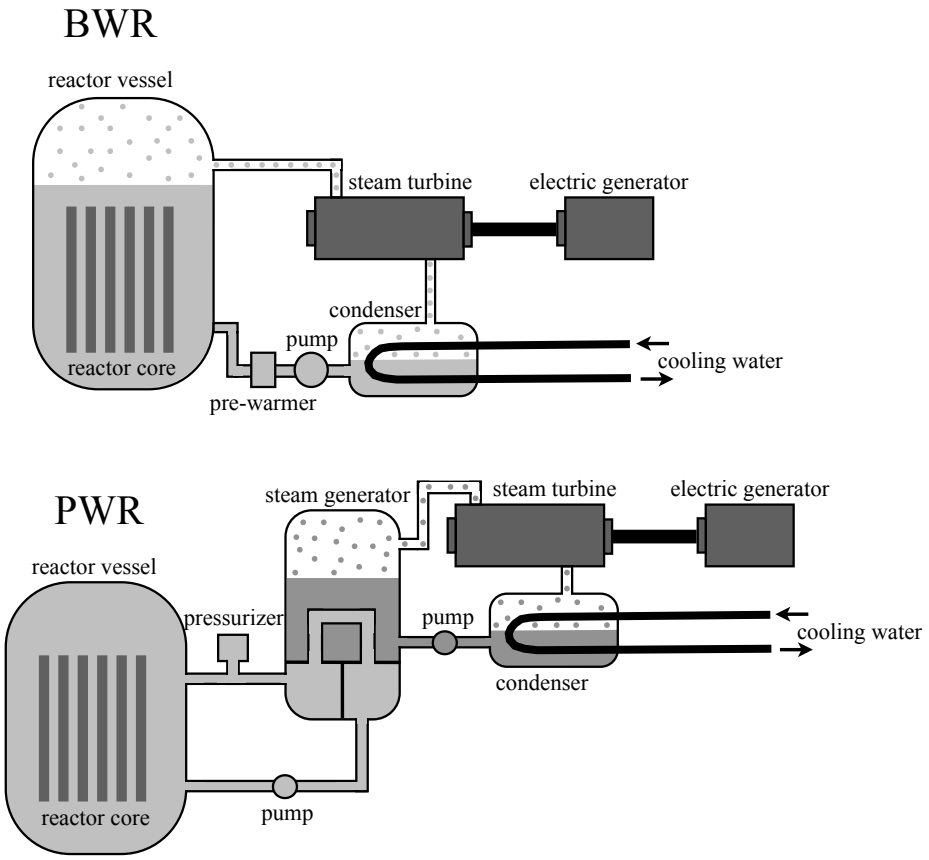

Figure 2.1: *Illustration of the main component in a boiling water reactor (BWR) and a pressurized water reactor (PWR).*

energy of ~ 2 MeV [17]. The probability of a fission reaction to occur depends on the energy of the incoming neutron. Fast neutrons have a very low probability to induce new fission events. To increase the probability of a fission event these neutrons have to be converted into thermal neutrons with an energy of ~ 0.025 eV [17]. Fast neutrons are slowed down to thermal neutrons by the water in the reactor core that acts as moderator. Fuel in a LWR consists of uranium dioxide (UO_2) that are put in small cuts. The uranium is enriched to have a ^{235}U concentration of 3-5 % [17]. The cuts are placed into long tubes of zirconium and several tubes constitutes a fuel bundles. The cladding tubes separate the fuel and the coolant water in order to contain the fission products and transfer heat from fuel to coolant. In order to have a self-sustained nuclear core, neutrons that are

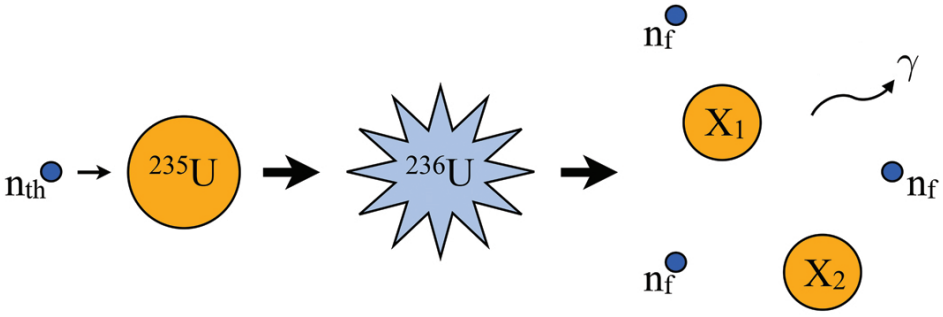

Figure 2.2: *Schematic representation of the fission reaction. A thermal neutron n_{th} collides with a ^{235}U nucleus and an unstalble ^{235}U nucleus is formed that is decomposed into two nuclei X_1 and X_2, 2-3 fast neutrons n_f, and γ-radiation.*

produced by fission reactions must induce new fission events and not be absorbed by components in the core. One main advantage of zirconium alloys as component material in reactor cores is zirconium's low cross section for absorbing thermal neutrons. Even though the effect of thermal neutrons on zirconium is very low, zirconium undergoes strong irradiation damage due to fast neutrons. The irradiation causes creep and growth in the zirconium components in the reactor, e.g. fuel-rod elongation, and BWR channel bow [18]. This has to be taken into consideration in the operation of the reactor as well as in the fabrication process of zirconium components.

2.2 Zirconium

Zirconium is an element found in the earth's crust with an abundance of 160 ppm [19] and it is the fourth most abundant transition metal after Fe, Ti and Mn [19]. Zirconium is most commonly found in the ores zircon ($ZrSiO_4$) and baddeleyite (ZrO_2) [20]. Zirconium and zirconium oxides are of major technological importance. There are broad applications for these materials, from cladding in nuclear power plant and as fuel cell electrolyte [21] to semiconductors [22] and in hip-implants [23]. Another advantage with zirconium is good corrosion resistance at reactor conditions. Zirconium ores contain between 1.5-2.5 % hafnium and this has to be removed before it is used for nuclear applications [24] due to hafnium's high neutron cross section.The probablity for a neutron capture reaction in Hf is 560 times larger compared to Zr [25]. The product chain for zirconium sponge follows as [24, 26, 27]:

1. Zircon is converted into hafniated zirconium tetrachloride.
2. Sublimate of hafniated zirconium tetrachloride is produced.
3. Zirconium tetrachloride and hafnium tetrachloride is separated.
4. The purified zirconium tetrachloride is converted into zirconium sponge containing Mg through the Kroll process by $ZrCl_4 + 2\,Mg = Zr + 2\,MgCl_2$. Excess magnesium is removed.
5. Production of Zr sponge through crumble and milling.

The zirconium sponge is melted in an electric arc furnace to produce zirconium ingots where alloying elements are added. The ingot is forged. Thereafter, a thermochemical process take place that include hot forging, water quenching, extrusion, cold-rolling and annealing. Cold-rolling and annealing steps are crucial for final secondary phase particle properties, and thus also for the hardness and corrosion properties of the alloy. The process where zirconium is extracted from ore is expensive mainly due to the need for an oxygen free environment as well as the removal of hafnium [24]. In addition, zirconium used in the nuclear industry has stringent requirements due to safety issues, therefore extensive controls are needed during the fabrication process.

2.3 Microstructure

Pure zirconium is found as α-Zr at temperatures below 863° C and as β-Zr for higher temperatures [28]. α-Zr has a hexagonal close-packed (hcp) structure, see Fig. 2.3, that is slightly compressed in the *c*-direction with a *c/a* ratio of 1.593 compared to the ideal ratio of 1.633 for hcp lattices [24]. The lattice parameters are $a_0 = 0.323$ nm and $c_o = 0.515$ nm [29]. β-Zr has a body centered cubic structure. α-Zr exhibits strong anisotropic behavior, the difference in the thermal expansion and Young's modulus between the *a*- and *c*-directions gives rise to internal stresses [24]. The orientation of the grains influence the behavior in the reactor. For example, the oxygen diffusion is different in the *c*-direction compared to the *a*-direction.

Zirconium dioxide is found in three phases: monoclinic, tetragonal and cubic, where $m-ZrO_2$ is the stable phase at ambient conditions. The $m-ZrO_2$ phase is the phase most dominant in the cladding tube oxide, but $t-ZrO_2$ is also present [30–35]. Highest fraction of the tetragonal phase is observed close to the metal/

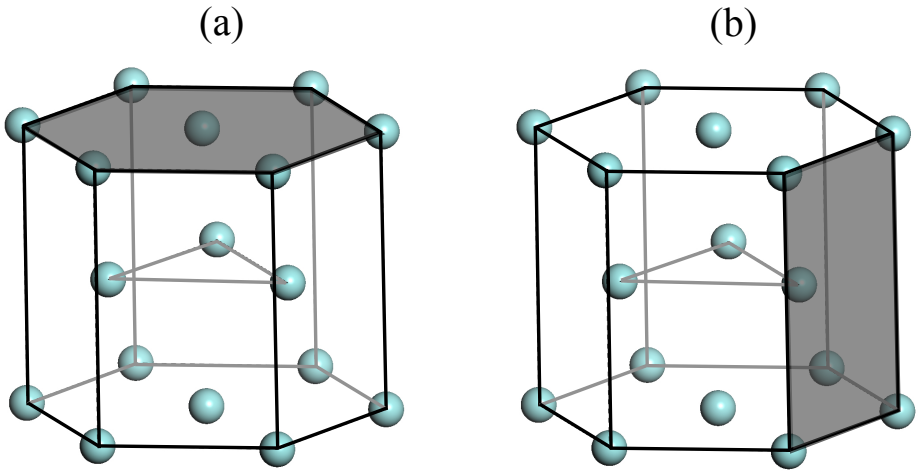

Figure 2.3: *The hexagonal closed packed (hcp) structure of zirconium. The shaded area in (a) is a basal plane and the shaded area in (b) is a prismatic plane.*

oxide interface [30, 33, 35]. The tetragonal phase is stabilized by a combination of small grain size, pressure and alloying elements [31, 33, 35, 36]. Conditions in the cladding tubes stabilize a suboxide layer at the metal/oxide interface. This has been reported to have a composition close to ZrO and has been observed by Atom Probe Tomography (APT) [37, 38] and Electron Energy Loss Spectroscopy (EELS) [37, 38]. The presence and thickness of this layer vary much between different samples. Recently, Puchala and Van der Ven [39] predicted a hexagonal ZrO structure from DFT modelling. This has been confirmed by Nicholls et al [40] that found this structure most stable and fit to diffraction and EELS data. Hu et al. have observed this phase by transmission-EBSD (Electron Back Scatter Diffraction) [41]. An oxygen saturated region is observed further away from the oxide/metal interface with varying oxygen concentration between 0-30 at.%. Thermodynamically, zirconium can dissolve oxygen to very high concentrations compared to many other metals. The solubility limit is reported to 29 at.% [28].

2.4 Zirconium alloys for cladding of nuclear fuel

Materials that are used in a nuclear reactor core have to withstand an aggressive environment and satisfy strict safety conditions. From the outside, the cladding tube is exposed to water at temperatures ranging between 280 °C to 350 °C de-

pending on reactor type [24]. From the inside, the cladding tube is exposed to fission products, a temperature of $\sim 400^{\circ}$ C and different types of radiation [24]. Especially, neutron irradiation is a large source of irradiation induced defects in the cladding tube material.

There are different types of zirconium alloys that are used as cladding material of nuclear fuel. Alloying elements are added to zirconium in order to improve corrosion resistance and mechanical strength. Alloying elements have a large impact on the corrosion properties, and are influenced by e.g. heat treatment of the alloy and external parameters like the different operation conditions of a BWR and a PWR. The most important alloying elements are iron, chromium, nickel, tin, and niobium and composition of the most used alloys are listed in Table 2.1.

Table 2.1: *Nominal composition of the most common commercial zirconium alloys [27]. The composition is given in weight percent or ppm. (Zry is a short form for zircaloy).*

Alloy	Sn	Nb	Fe	Cr	Ni	O	S
Zry-2	1.2-1.5	-	0.07-0.2	0.1	0.05	0.12	-
Zry-4	1.2-1.7	-	0.18-0.24	0.1	-	0.1-0.14	10-35 ppm
M5	-	0.8-1.2	<500 ppm	-	-	0.11-0.16	-
E110	-	1	100 ppm	-	-	0.05-0.07	-
Zr-2.5Nb	-	2.5-2.7	<650 ppm	-	-	0.12-0.15	-
E123	-	2.5-2.6	-	-	-	0.04-0.07	-
ZIRLO	1	1	0.1	-	-	0.09-0.12	-
E635	1.2	1	0.35	-	-	0.05-0.07	-

2.4.1 Tin

Tin influences mechanical properties of the alloy, in that it increases the yield strength of the alloy [24]. Tin is also an α-Zr stabilizer [42] and it is known to stabilize the tetragonal ZrO_2 phase during corrosion [35]. In commercial alloys, tin does not form precipitates since it is fully soluble in the zirconium matrix [42]. Tin was first added to counter the poor corrosion resistance caused by nitrogen impurities, but tin has both positive and negative effects on the corrosion behavior [43]. Today, the trend is to decrease the tin content in alloys used in PWR as e.g. in Optimized ZIRLO^{TM}and low tin Zircaloy-4 [35].

2.4.2 Iron, nickel and chromium

Iron, nickel and chromium are used to increase corrosion resistance. They display low solubility in α-Zr and are mainly found as intermetallic precipitates [36]. These second phase particle (SPP) have a large impact of the corrosion behavior. It is known from trial and error that these precipitates improve the corrosion resistance but the reason behind is unknown. There are several studies giving possible explanations of the role of SPP. Parameters affecting the oxidation behavior are precipitate size [44–46], crystal structure of the precipitates [47], and thermodynamic properties for oxidation of the elements constituting the precipitates [48–50]. An additional effect of SPPs are that they, in general, have a slower oxidation rate compared to the surrounding matrix [38, 44, 45]. The delayed oxidation give rise to crack formation in the oxide [50, 51]. Not all iron, nickel and chromium are found in SPP. These are also found to segregate to grain boundaries and other defects [52].

2.4.3 Niobium

Niobium is known to delay transition in the oxidation cycle [53]. Nb is very sensitive to the heat treatment of the alloy and has low solubility in α-Zr matrix and diffuses very slowly in Zr, so the annealing time is decisive for if Nb is found dissolved in the matrix or as precipitates [24, 27]. Also, Nb has positive effects on mechanical properties and on corrosion resistance [27].

2.4.4 Oxygen and sulfur

Oxygen is considered as an alloying element and not an impurity. Oxygen is an α-Zr stabilizer and is added to increase the yield strength without degradation of corrosion resistance [24]. The use of oxygen for strengthening is rare in metallurgy, commonly nitrogen is used but in the zirconium case nitrogen is avoided since it cause severe corrosion [27].

In recent years, sulfur has been found to improve creep resistance, even at as low concentrations as 30-50 ppm [27]. Sulfur atoms is segregated into the core of dislocations and does not affect the corrosion properties.

Chapter 3

Corrosion of zirconium

Corrosion of zirconium has been an active research field since the 1950's. New alloys with better corrosion properties results in more efficeint utilisation of the nuclear fuel when the fuel can be in the reactor core longer timeperiods. Zirconium oxidation with water as corrodent is a complicate process and there are many factors that have to be taken into account when optimize the corrosion properties. Cyclic oxidation rate behaviour and hydrogen pick-up are two examples of such factors.

3.1 Oxide growth

Water oxidation of zirconium alloys is a complex phenomenon and can be described by cyclic sub-parabolic mass gain curve each terminated by transition to the next cycle, see Fig. 3.1. Each cycle may build a few μm of oxide prior to undergoing transition. Oxygen diffusion in ZrO_2 is much faster than diffusion of Zr, resulting in a inwards growing oxide [54]. The oxide ions have to diffuse from the water/oxide interface through the oxide to the oxide/metal interface where new ZrO_2 is formed. This results in that stresses are build up at the metal/oxide interface since the Pilling Bedworth ratio is 1.55 [55], i.e. the volume unit of the oxide is 1.55 times larger compared to the volume unit of the metal. The point where the protective oxide breaks the first time is important in corrosion research and is called transition, i.e. where the second cycle starts. The time period before this point is called pre-transition, and the time period after is called post-transition. The behavior is repeated in cycles with several transitions, but after some cycles the oxidation rate becomes linear [56, 57]. The cyclic behavior

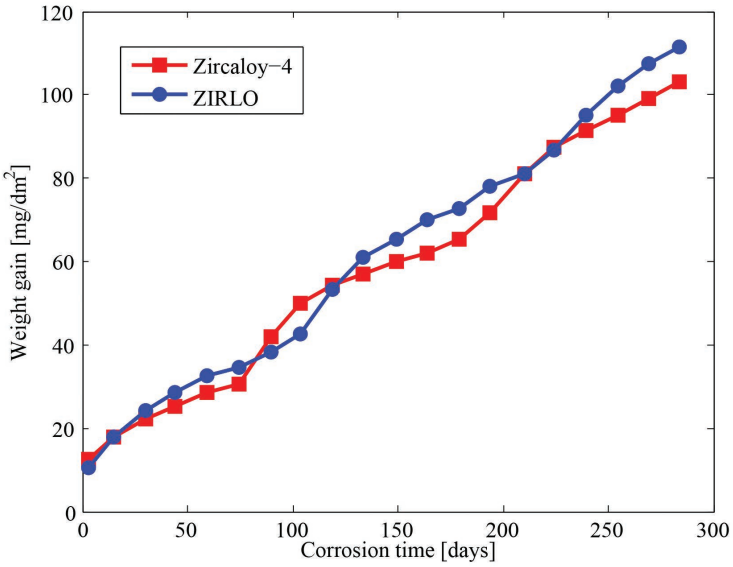

Figure 3.1: *Corrosion weight gain versus exposure time in* 360° *C water for ZIRLO TM and Zircaloy-4. Redraw from de Gabory et al. [38].*

is most prominent for the alloy Zircaloy-4 where several cycles can be observed before the linear behavior becomes dominant [57, 58]. The time to transition varies between different alloys.

Time dependence of the oxide growth can be described by a power law,

$$w = At^n \tag{3.1}$$

where w is the weight gain in mg/dm^2, t the oxidation time in days, A and n are constants that are dependent on the alloy and oxidizing conditions. w can also be the oxide thickness. For typical zirconium alloys $n < 0.5$, i.e. they have a subparabolic behavior. The deviation from parabolic behavior is generally associated with that the electron conductivity is rate limiting and not the ion diffusion. The oxidation rate is fast from the beginning when the oxide scale is so thin that electrons can tunnel through the oxide scale and decrease as the oxide becomes thicker. This decrease in oxidation rate is due to that the first formed ZrO_2 is building a protective scale that is a large band gap isolator. The exponent n from pre-transition power law fits to the data in Fig. 3.1 gives $n = 0.3$ and $n = 0.4$ for Zircaloy-4 and ZIRLO, respectively.

It is not completely understood why the transitions occur but there are several theories, e.g. coalescence of small pores [59] or accumulation of stress [60]. Both pores [61, 62] and build up of stresses [63, 64] have been observed, but there are no explanation of how this would affect differently in different alloys [65]. Another theory is proposed by Harada *et al.* [66]. They have observed a change in hydrogen profile in the oxide layer before and after transition, and suggest that phase stability of the interface layer are affected by hydrogen.

3.2 Hydrogen pick-up

In order to have an ongoing corrosion process of a zirconium alloy with water, reduction of protons from H_2O molecules are necessary since oxidation of O^{2-} ions are needed to form ZrO_2. The fate of the hydrogen is dual, either H_2 can be formed and be released in the water or H can be incorporated in the metal underneath the oxide scale. This phenomenon is called hydrogen pick-up (HPU). It is the hydrogen pick-up fraction (HPUF) that is studied in order to quantify the alloy dependence on how much hydrogen that is incorporated in the metal. Hydrogen pick-up is along with the oxidation rate decisive for the time the nuclear fuel can be inside the reactor. HPUF is the fraction of hydrogen that are absorbed in the metal compared to the total amount of hydrogen that is produced in the oxidation process,

$$HPUF = \frac{[H]_{\text{absorbed}}}{[H]_{\text{produced}}}. \tag{3.2}$$

Hydrogen solubility in the zirconium matrix is very low. If the hydrogen content becomes higher than this limit precipitates form, i.e. zirconium hydrides [67]. These hydrides can eventually cause hydrogen embrittlement, as the already low solubility decreases upon cooling. The problem with hydrogen embrittlement becomes more severe for fuel rod claddings when the fuel is taken out from the reactor. When the zirconium cools hydride forms, migrates to and accumulates in regions under stress and with steep temperature gradients. This is called delayed hydride cracking [68].

There is a general trend in the nuclear industry to increase the burnup of the fuel, i.e. to increase the time that the fuel stays in the reactor. This is why the oxidation of the zirconium alloys and the HPU are decisive for how long the fuel can be in the reactor. Mechanisms controlling how the instantaneous hydrogen pick-up in

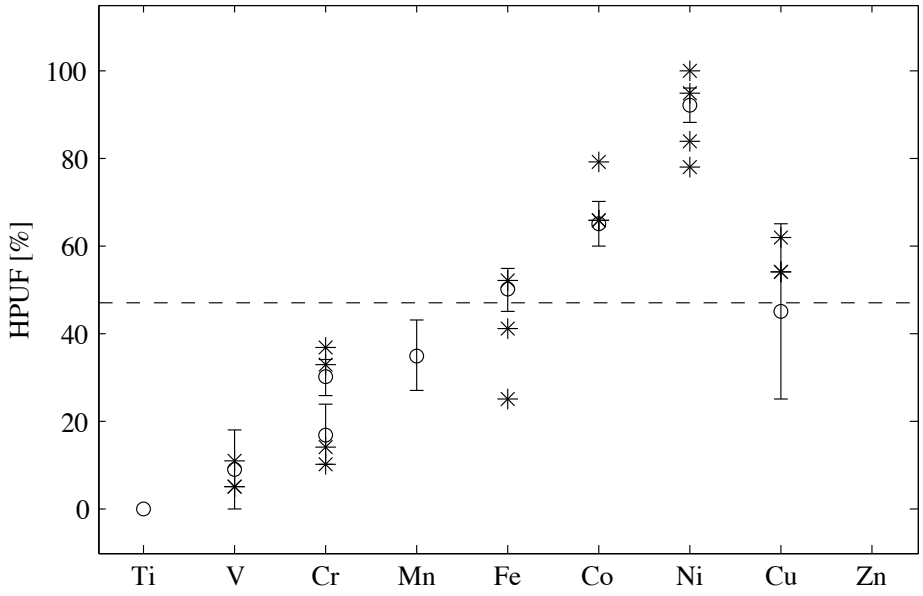

Figure 3.2: *HPUF for some binary alloys. ∘ from [80] and ∗ from [79]. The horizontal line corresponds to sponge Zr [79].*

zirconium alloys are not understood and it is influenced by many factors. Two examples are water chemistry and chemical composition of the alloy. The hydrogen pick-up fraction changes during the oxidation cycle [66, 69, 70]. In general, HPUF is high when the oxidation rate is low, increases when the oxidation rate decreases, and peaks just before transition when the oxidation rate is almost zero. There are many different theories about the ingress of hydrogen through the barrier layer in the oxide. One theory is based on that hydrogen migrates through the oxide barrier through pores and cracks [71–73]. Other theories propose that protons or OH^- migrate through the oxide lattice [74, 75], or via second-phase particles [76, 77].

The addition of alloying elements in the zirconium alloy has a large impact of the hydrogen pick-up fraction [78–80], some elements decrease the HPUF and some increase the HPUF. In Fig. 3.2 the elemental dependence for some binary alloys are displayed. In alloys with more than two elements, the ratio between the alloying elements has a large effect of the HPUF. Alloys with Ni display higher HPUF compared to similar alloys without Ni. There are several studied of the

impact of the ratio of the alloying elements. Two examples are that the HPUF decreases with increasing Fe/Ni ration for Zr-Sn-FeCrNi [81], and the HPUF increases with corrosion resistance of a Zr-Sn-FeCr alloys with a Cr content of <0.15% [82].

When trying to find a connection of the hydrogen pickup and the corrosion mechanism it is the instantaneously HPUF that is interesting. This is the fraction of absorbed hydrogen between successive measurements. Haranda and Wakamatsu [66] report of a relation between HPU and the transition in the oxidation curve. There data present a peak in the instantaneous HPUF just before transition with a rapid drop after the transition. Similar results have been reported by Couet *et al.* [69, 70].

Chapter 4

Quantum chemistry

Quantum chemistry is a branch in chemistry that uses quantum mechanics to investigate and explore chemical systems. The development of computational methods and more powerful computers the last decades have made quantum-mechanical methods an important tool to e.g. study molecular structures, and spectroscopic parameters as help to interpret spectroscopic measurements.

4.1 Schrödinger equation

The fundamental equation in quantum chemistry is the Schrödingier equation that was introduced by Erwin Schrödeinger in 1926 [83]. This was the time-dependent non-relativistic Schrödingier equation,

$$\hat{H}\Psi(\mathbf{r},t) = i\hbar\frac{\partial\Psi(\mathbf{r},t)}{\partial t}, \tag{4.1}$$

that was inspired by Hamilton-Jacobi formalism for classical mechanics and the wave description of electrons introduced by de Broglie. H is the Hamiltonian and Ψ is the wave function. In a majority of all quantum chemical calculations it is the time independent Schrödinger equation that is used,

$$\hat{H}\psi(\mathbf{r}) = E\psi(\mathbf{r}). \tag{4.2}$$

$\psi(\mathbf{r})$ is the wave function that only has a $\mathbf{r}$-dependence. This is obtained by setting $\Psi(\mathbf{r},t) = \psi(\mathbf{r})f(t)$ in Eq. 4.1 and use the procedure of variable separation so that the left-hand side of the equation has a $\mathbf{r}$-dependence and the right-hand

side only has a t-dependence. Thus, both sides have to be equal to a constant E. The $\mathbf{r}$-dependent side gives Eq. 4.2 and from the t-dependent side $f(t)$ is obtained,

$$\Psi(\mathbf{r},t) = \psi(\mathbf{r})f(t) = \psi(\mathbf{r})e^{-i\frac{Et}{\hbar}}. \tag{4.3}$$

From Eq. 4.2, the energy, E, of a many particle system can be obtained. The wave function for a many particle system, $\psi(\mathbf{r_1},\mathbf{r_2},...,\mathbf{r_N})$, is dependent on the coordinates for the n particles in the system. H is the total non-relativistic Hamiltonian for a system of charged particles and can be divided into T_{nuc}, V_{N-N} and H_{el}. T_{nuc} is the kinetic energy of the nucleus in the system and V_{N-N} is the coulomb forces between nuclei. H_{el} is the electronic Hamiltonian that consist of the kinetic energy of the electrons and coulomb forces between the electrons, and between the nuclei and electrons,

$$\begin{aligned} H &= T_{nuc} + V_{N-N} + H_{el} = \\ &= \underbrace{-\sum_A \frac{1}{2m_A}\nabla_A^2}_{T_{nuc}} + \underbrace{\sum_{A<B} \frac{Q_A Q_B}{|\mathbf{R}_A - \mathbf{R}_B|}}_{V_{N-N}} \underbrace{-\sum_a \frac{1}{2}\nabla_a^2 + \sum_{a<b} \frac{1}{|\mathbf{r}_a - \mathbf{r}_b|} - \sum_{Aa} \frac{Q_A}{|\mathbf{R}_A - \mathbf{r}_a|}}_{H_{el}}. \end{aligned} \tag{4.4}$$

a and b are index of electrons and A and B are index of nuclei. $\mathbf{r}$ are electron coordinates and $\mathbf{R}$ are nuclear coordinates. In this equation and onwards atomistic units are used where $\hbar = 1$, $m_e = 1$, $q_e = 1$ and $\frac{1}{4\pi\varepsilon_0} = 1$. In addition, the nucleus mass m_A is expressed in electron mass m_e. From this, it would in principle be possible to solve any quantum chemical problem exactly given a Hamiltonian for the system. Due to the electron correlations the many-body wave function becomes too complicated to handle and approximations are needed. The first and most basic approximation is the Born-Oppenheimer approximation [84].

With the Born-Oppenheimer approximation, the total wave function is approximated as a product of a wave function of the nuclei, ϕ, and a wave function of the electrons, χ, giving the Born-Oppenheimer wave function ψ_{BO},

$$\psi_{BO}(\mathbf{r},\mathbf{R}) = \phi(\mathbf{R})\chi(\mathbf{r};\mathbf{R}), \tag{4.5}$$

The kinetic energy of the nucleus in the system, T_{nuc}, is only dependent on the coordinates of the nuclei and can be treated separately. The electronic energy E_{el} can be obtained from the electronic Hamiltonian H_{el} and the electronic wave function χ according to

$$\hat{H}_{el}(\mathbf{r},\mathbf{R})\chi(\mathbf{r};\mathbf{R}) = E_{el}(\mathbf{R})\chi(\mathbf{r};\mathbf{R}). \tag{4.6}$$

χ is dependent on both electron and nuclear coordinates. The nuclear wave function $\phi(\mathbf{R})$ is a solution to

$$\left\{\hat{T}_{nuc}(\mathbf{R}) + E_{el}(\mathbf{R}) + V_{N-N}(\mathbf{R})\right\}\phi(\mathbf{R}) = E\phi(\mathbf{R}). \tag{4.7}$$

The Born-Oppenheimer approximation is not valid if nuclear movements cause transitions between different electron states, then the total wave function cannot be separates into a wave function of the nuclei and a wave function of the electrons. Even though the Born-Oppenheimer approximation is a very important simplification of the molecular Schrödinger equation further approximation is needed.

4.2 Hartree-Fock equation

One of the first approximations that were used to calculate a many-electron system from first principles was the Hartee-Fock equation. It was first introduced by Hartree [85, 86] and later improved by Fock [87] and by Slater [88]. The heart of the approximation is that the electrons are treated as independent and non-coupled.

By introducing the Hartree product, the wave function for a many-electron system $\psi(\mathbf{r}_1, \mathbf{r}_2, \mathbf{r}_3, ..., \mathbf{r}_n)$ is written as a product of one-electron orbitals $\varphi_i(\mathbf{r}_i)$,

$$\psi(\mathbf{r}_1, \mathbf{r}_2, \mathbf{r}_3, ..., \mathbf{r}_n) = \varphi_1(\mathbf{r}_1)\varphi_2(\mathbf{r}_2)\varphi_3(\mathbf{r}_3)...\varphi_n(\mathbf{r}_n) \tag{4.8}$$

The Hartree product is not antisymmetric and is therefore not satisfactory for fermions (e.g. electrons). This can be fixed by introducing the Slater determinant [89],

$$\psi = (n!)^{-1/2}\begin{bmatrix} \varphi_1(\mathbf{r}_1) & \varphi_2(\mathbf{r}_1) & \cdots & \varphi_n(\mathbf{r}_1) \\ \varphi_1(\mathbf{r}_2) & \varphi_2(\mathbf{r}_2) & \cdots & \varphi_n(\mathbf{r}_2) \\ \vdots & \vdots & \ddots & \vdots \\ \varphi_1(\mathbf{r}_n) & \varphi_2(\mathbf{r}_n) & \cdots & \varphi_n(\mathbf{r}_n) \end{bmatrix} \tag{4.9}$$

The total electronic energy for a Slater determinant wave function can be obtained from the expectation value of the exact non-coupled Hamiltonian,

$$E = \left\langle \psi | \hat{H} | \psi \right\rangle. \tag{4.10}$$

The electronic Hamiltonian for a many-electron system can be written in terms of one-electron (h_a) and two electron terms (g_{ab}),

$$H = -\sum_{a}^{n} \underbrace{\Big(-\frac{1}{2}\nabla_a^2 - \sum_A \frac{Q_A}{|\mathbf{R}_A - \mathbf{r}_a|} \Big)}_{h_a}, + \sum_{a<b}^{n} \underbrace{\frac{1}{|\mathbf{r}_a - \mathbf{r}_b|}}_{g_{ab}} \tag{4.11}$$

where n is the number of electrons. Now, only the orbitals in the Slater determinant have to be known in order to determine the total energy. The orbitals are expressed with basis functions χ_μ according to

$$\varphi_i(\mathbf{r}) = \sum_{\mu}^{N} c_{i\mu}\chi_\mu(\mathbf{r}). \tag{4.12}$$

where N is the size of the basis set. Minimize E with the constraint of orthonormal orbitals leads to the Hartree-Fock equation,

$$\Big(-\frac{1}{2}\nabla^2 - \underbrace{\sum_A \frac{Q_A}{|\mathbf{R}_A - \mathbf{r}|}}_{V_{ext}} + \hat{J} - \hat{K} \Big) \varphi_i(\mathbf{r}) = \varepsilon_i \varphi_i(\mathbf{r}) \tag{4.13}$$

where J is the Coulomb operator, K is the exchange operator and ε_i are orbital energies. This equation is solved iteratively on matrix form,

$$\mathbf{FC} = \mathbf{SC}\varepsilon, \tag{4.14}$$

with Eq. 4.12. $\mathbf{C}$ from previous iteration is employed to form a new $F_{\mu\nu}$. In every iteration, the secular equation is solved to produce a new set of orbitals and a new set of orbital energies ε_i. This is solved using

$$S_{\mu\nu} = \int \chi_\mu(\mathbf{r})^* \chi_\nu(\mathbf{r}) d^3\mathbf{r} \tag{4.15}$$

and

$$F_{\mu\nu} = <\chi_\mu|\hat{h}|\chi_\nu> + \sum_{\gamma\delta} D_{\gamma\delta} \big\{ <\chi_\mu\chi_\gamma|\chi_\nu\chi_\delta> - <\chi_\mu\chi_\nu|\chi_\gamma\chi_\delta> \big\} \tag{4.16}$$

with

$$h = -\frac{1}{2}\nabla^2 - \sum_A \frac{Q_A}{|\mathbf{R}_A - \mathbf{r}|} \tag{4.17}$$

$$<\chi_\mu|\hat{h}|\chi_\nu> \equiv \int \chi_\mu(\mathbf{r})^* h \chi_\nu(\mathbf{r}) d^3\mathbf{r} \tag{4.18}$$

$$D_{\gamma\delta} = \sum_{i}^{N_{occ}} C_{i\gamma} C_{i\delta} \tag{4.19}$$

$$< \chi_\mu \chi_\gamma | \chi_\nu \chi_\delta > \equiv \iint \chi_\mu(\mathbf{r})^* \chi_\gamma(\mathbf{r}')^* \frac{1}{|\mathbf{r}-\mathbf{r}'|} \chi_\delta(\mathbf{r}) \chi_\nu(\mathbf{r}') d^3\mathbf{r} d^3\mathbf{r}'. \tag{4.20}$$

The total energy can be obtained from the sum of all orbital energies with compensation for the Coulomb and exchange term,

$$E = \sum_{i}^{n} \varepsilon_i - \frac{1}{2} \sum_{ij}^{n} \left\{ \underbrace{\langle \varphi_i \varphi_j | \varphi_i \varphi_j \rangle}_{\text{Coulomb term}} - \underbrace{\langle \varphi_i \varphi_j | \varphi_j \varphi_i \rangle}_{\text{exchange term}} \right\}. \tag{4.21}$$

The total energy can also be expressed as

$$E = \sum_{i}^{n} \langle \varphi_i h \varphi_i \rangle + \frac{1}{2} \sum_{ij}^{n} \left\{ \langle \varphi_i \varphi_j | \varphi_i \varphi_j \rangle - \langle \varphi_i \varphi_j | \varphi_j \varphi_i \rangle \right\}. \tag{4.22}$$

The energy of a many-electron system can be calculated but it takes a large amount of computer time and memory. The Hartree-Fock method scales nominally as N^4 where N is the size of the basis set.

4.3 Density Functional Theory

Density functional theory (DFT) is a complementary way to receive information about a many-electron system. DFT is based on two theorems introduced by Hohenberg and Kohn [15]. It is not the electron position that are used to obtain quantum mechanical properties, instead it is the electron density, $\rho(\mathbf{r})$, that is employed. The electron density is correlated to the wave function according to

$$\rho(\mathbf{r}) = \psi^*(\mathbf{r})\psi(\mathbf{r}) = |\psi(\mathbf{r})|^2. \tag{4.23}$$

The main advantage of DFT is that accurate results can be obtained for relative little computational cost. DFT scales nominally as N^2.

The Hohenberg-Kohn theorem states

1. The external potential, $v_{ext}(\mathbf{r})$, uniquely determine the ground state density $\rho_0(\mathbf{r})$, i.e. there is a one-to-one relationship between the external potential and the electron density,

$$v_{ext}(\mathbf{r}) \overset{1\text{ - }1}{\longleftrightarrow} \rho_0(\mathbf{r}). \tag{4.24}$$

2. There exists a density functional $E_{HK}[\rho]$ with the following properties:

$$E_{HK}[\rho] > E_0 \text{ for } \rho \neq \rho_0, \tag{4.25}$$

$$E_{HK}[\rho_0] = E_0. \tag{4.26}$$

The solution to the Euler-Lagrange equation

$$\frac{\delta}{\delta\rho(\mathbf{r})} E_{HK}[\rho]\Big|_{\rho=\rho_0} = 0 \tag{4.27}$$

yields the ground-state density $\rho_0(\mathbf{r})$ of the system. The definition of the energy functional is

$$E_{HK}[\rho] = \int v_0(\mathbf{r})\rho(\mathbf{r})d^3\mathbf{r} + \underbrace{\int \psi^*[\rho]\left(\hat{T}+\hat{U}\right)\psi[\rho]d^3\mathbf{r}}_{F[\rho]}. \tag{4.28}$$

It is the external potential v_0 that determines the system and $F[\rho]$ is universal. $F[\rho]$ consists of kinetic energy of the electrons and electron-electron interactions. Given that all terms would be known, then the exact energy of a system could be calculated. The method mainly used to determine the electron density is based on the so called Kohn-Sham equation [16],

$$\left(-\frac{\nabla^2}{2} + V_{ext}(\mathbf{r}) + \underbrace{\int \frac{\rho(\mathbf{r})}{|\mathbf{r}-\mathbf{r}'|}d^3\mathbf{r}'}_{v_H} + V_{xc}[\rho]\right)\varphi_i(\mathbf{r}) = \varepsilon_i\varphi_i, \tag{4.29}$$

where φ_i is Kohn-Sham orbital and ε_i is the orbital energy. The true external potential for interacting electrons is replaced by an effective local potential $v_{KS,0}$ for non-interacting electron. The Kohn-Sham equation can only be used if the system is v-representable. A system is v-representable if $v_0(\mathbf{r})$ are an external potential with the corresponding ground-state $\rho_0(\mathbf{r})$ for interacting particles, and if the effective local potential $v_{KS,0}(\mathbf{r})$ for non-interacting particles corresponds to the same ground state density $\rho_0(\mathbf{r})$, see Fig 4.1. $V_{xc}[\rho_0]$ is defined as

$$V_{xc}[\rho_0] = \frac{\delta E_{xc}[\rho]}{\delta\rho}\Big|_{\rho_0} \tag{4.30}$$

and

$$\rho_0 = \sum_i^{N_{occ}} |\varphi_i|^2, \tag{4.31}$$

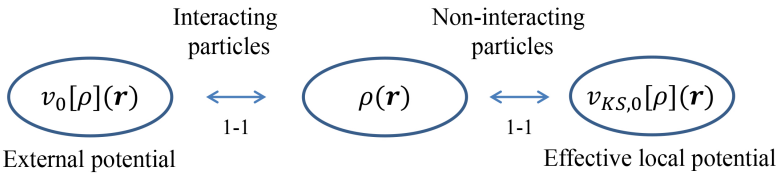

Figure 4.1: *Schematic representation of the relation between the external potential* $v_0(\mathbf{r})$ *with the corresponding ground-state* $\rho_0(\mathbf{r})$ *for interacting particles and the local potential* $v_{KS,0}(\mathbf{r})$ *for non-interacting particles.*

where the sum is over all occupied states. The exchange-correlation energy, E_{xc}, is defined as

$$E_{xc}[\rho] = F[\rho] - \frac{1}{2}\iint \frac{\rho(\mathbf{r})(\mathbf{r}')}{|\mathbf{r}-\mathbf{r}'|} d^3\mathbf{r} d^3\mathbf{r}' - T_s[\rho] \tag{4.32}$$

and T_s is the kinetic energy of non-interacting electrons. The total energy is obtained from Eq. 4.28 where

$$F[\rho] = T_s[\rho] + V_{\mathrm{H}}[\rho] + E_{xc}[\rho]. \tag{4.33}$$

The total energy consists of four parts:

$\mathbf{E_{ext}}$ Energy contribution from the external field on the electrons caused by the position of the nuclei.

$\mathbf{T_s}$ Kinetic energy of non-interacting electrons.

$\mathbf{V_H}$ Hartree energy of the classical electron-electron Coulomb potential.

$\mathbf{E_{xc}}$ Exchange-correlation energy that includes the non-direct electron-electron interaction as well as the difference between T_s and the true kinetic energy of the electronic system.

The total energy can be expressed as

$$\begin{aligned} E[\rho] = &\int v_{KS,0}(\mathbf{r})\rho(\mathbf{r}) d\mathbf{r} + \sum_{i=1}^{N} \left(\int \varphi_i^* \left(-\frac{1}{2}\nabla^2 \right) \varphi_i d^3\mathbf{r} \right) + \\ &+ \frac{1}{2}\iint \frac{\rho(\mathbf{r})\rho(\mathbf{r}')}{|\mathbf{r}-\mathbf{r}'|} d^3\mathbf{r} d^3\mathbf{r}' + E_{xc}[\rho], \end{aligned} \tag{4.34}$$

and is solved iteratively, see Fig. 4.2. This is done with the same procedure as with the Hartree-Fock equation, see Eq. 4.13 and 4.14. The Kohn-Sham equation

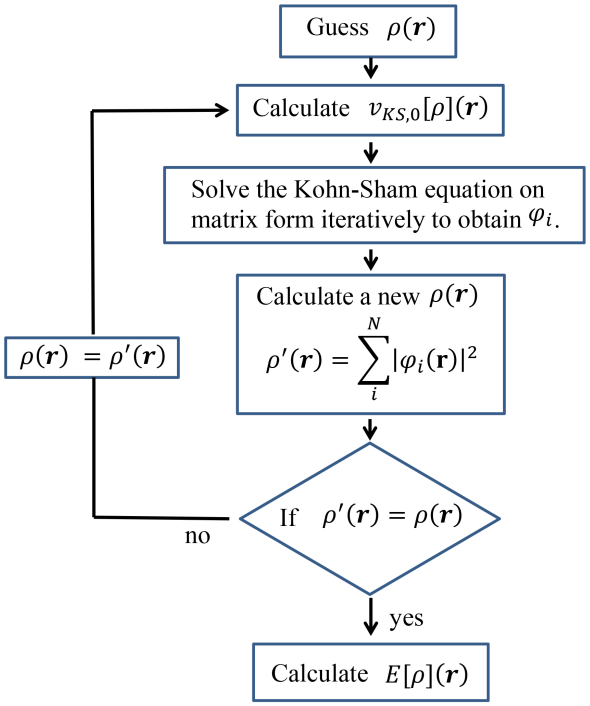

Figure 4.2: *Flow chart over the iterative procedure to calculate the total energy E. At the start, an electron density is guessed and used to calculate $v_{KS,0}$. This is used to solve the Kohn-Sham equation on matrix form iteratively to obtain φ_i, and is used to calculate a new electron density ρ'. A new $v_{KS,0}$ is calculated with the new electron density and the procedure continues until the new calculate electron density is equal to the electron density obtained in the previous iteration. At the end, the total energy is calculated with the converged electron density.*

is very similar to the Hartree-Fock equation, compare Eq. 4.29 and 4.13, the only difference is the exchange-correlation term in the Kohn-Sham equation and the exchange term in the Hartree-Fock equation. In the Kohn-Sham equation, it is possible to calculate the energy contributions from the kinetic term, the external potential term and the electron-electron Coulomb interaction term exactly, but it is very complicated to calculate the exchange-correlation functional $E_{xc}[\rho]$. Further approximations on how to calculate the $E_{xc}[\rho]$ are therefore needed.

4.4 Exchange-correlation functional

Critical for density functional theory calculations is the choice of exchange-correlation functional. A large number of approximations of the functional have been developed over the years. The most basic approximation is the local density approximation, LDA, that was introduced by Kohn and Sham [90]. Two examples of LDA functionals are the VWN functional by Vosko *et al.* [91] and the PWC functional by Perdew and Wang [92]. The electron density is approximated by a homogenous electron gas, i.e. the electron density is assumed to be the same at each point. This approximation is quite good for electronic systems that are strongly delocalized such as metals, but not so good for localized systems such as molecules where the electron density is strongly varying within the molecule.

The generalized gradient approximation, GGA, is an extension of the LDA approximation. The LDA approximation is improved by take into consideration variations in the electron density in the close proximity. This is accomplished by adding the gradient of the electron density to the LDA approximation. With this addition, the accuracy is improved to be acceptable for many chemical problems. The GGA functional are typically constructed by a separate exchange term and a correlation term. There exists several functional for GGA calculations, among others is the PBE functional by Perdew, Burke and Ernzerhof [93], the PW91 functional by Perdew and Wang [92] and the BLYP functional by Becke [94] and Lee *et al.* [95]. A further improvement is obtained by adding a certain amount of exact exchange taken from Hartree-Fock, compare Eq. 4.13 and Eq. 4.29. These are called hybrid functional and the most common used are the PBE0 functional by Adamo and Barony [96] and the B3LYP functional by Becke [97] and Stephens *et al.* [98].

There are two major problems with DFT that arise with the approximated exchange-correlation functional. These are the self-interaction error and an error resulting from the static correlation. The self-interaction error is a result of that electrons in DFT have a repulsive interaction with all electrons in the system including themselves. This results in a tendency to favor delocalized metallic states over local electron configurations [99]. A result of this is that band gaps calculated with GGA are underestimated. The problem with static correlation [100–102] arises from that the wave function is described by only a single determinant. This is a good description for systems that are non-degenerated, but for degenerated systems this is a bad description and thus a large error due to static correlation is expected.

4.5 Basis sets and pseudopotentials

In order to implement Kohn-Sham DFT in a computational code, basis sets are needed to express the Kohn-Sham orbitals. There are several basis sets available, including Slater functions [103], Gaussian functions [104], plane waves basis set [105, 106] and numerical basis set. In this study, both plane wave and numerical basis sets are used.

Throughout this study periodic boundary conditions have been used in conjunction with both plane wave and numerical basis sets. According to Bloch's theorem, the eigenstates of a system subject to a periodic potential can be written as

$$\varphi_j(\mathbf{r},\mathbf{k}) = e^{i\mathbf{k}\mathbf{r}} u_j(\mathbf{r}) \tag{4.35}$$

with

$$u_j(\mathbf{r}) = \sum_G C_{Gj} e^{i\mathbf{G}\mathbf{r}}. \tag{4.36}$$

The electronic wave function may at each k-point be expanded in terms of a plane wave basis set or by using the atom centered numerical basis set.

In principle, an infinite number of plane waves are required to span plane-wave basis set. Coefficient C_{k+G} for plane waves with lower kinetic energy, $|\mathbf{k}+\mathbf{G}|^2$, are more important compared to those with larger energy. This is used to truncate the basis set to only include plane waves with lower kinetic energy than a cutoff energy. From the truncation, a systematic error is introduced in the computed total energy and its derivatives. It is possible to decrease the error by increasing the cutoff energy to an increased computational cost.

The use of numerical basis set is a different approach to express the Kohn-Sham orbitals, where each basis function corresponds to an atomic orbital. The basis functions are given by numerical values on an atomic-centered spherical-polar mesh [107]. Atomic basis sets are confined within a cutoff value. By introducing an additional basis function and polarization an increased accuracy is achieved with the drawback of increased cost. At the minimal basis there are one atomic orbital for each occupied atomic orbital. A double numerical basis set introduce a second set of valence atomic orbital. Polarization d-function can be added to all non-hydrogen atoms and polarization p-function can be added to all hydrogen atoms that is important for hydrogen bonding.

To reduce the computational effort pseudopotentials are introduced. Electrons are subdivided into two groups: valence electrons and core electrons. The direct contribution from core electrons to the chemical binding can often be neglected besides screening the nuclear charge. Hence, pseudopotentials are introduced to mimic the effect of the core electrons on the valence electrons. Pseudopotentials are in general non-local in the sense that they utilize projection operators composed of the very atomic core orbitals that have been omitted. Thus, only the valence electrons are described explicitly in the Kohn-Sham energy optimization scheme. The pseudopotentials are analogous for numerical basis set as for plane wave basis set, the only difference is how the electronic wave function is expanded. A concept that is used to describe a pseudopotential is the hardness of the pseudopotential. A pseudopotential is soft when a small number of Fourier components are required to give a correct representation, and a pseudopotential is hard if a large number is required. Ultrasoft potentials are much softer than norm-conserving potentials resulting in a lower cutoff energy for ultrasoft potentials and a reduced computational effort. Cutoff energies are greatly reduced for ultrasoft pseudopotentials as compared to those for norm-conserving pseudopotentials. While computationally favored, the drawback with any truncation of the plane wave basis is that the description of the high-energy interface between pseudopotential and valence orbitals may be erroneously described. When performing calculations with a plane wave basis set, it is therefore important to increase the cutoff energy until the calculated total energy converges.

Norm-conserving pseudopotentials are such that

$$\int_0^{R_c} \varphi^2_{\text{all electron}} d^3\mathbf{r} = \int_0^{R_c} \varphi^2_{\text{pseudopotential}} d^3\mathbf{r} \tag{4.37}$$

where R_c is the core radius, $\varphi_{\text{all electron}}$ is an orbital obtained from an all electron calculation and $\varphi_{\text{pseudopotential}}$ is an orbital obtained from a pseudopotential calculation. A high cut-off energy is needed because details inside R_c are described by the plane-waves basis set.

For ultrasoft pseudopotentials, two components are introduced. One exclusively inside R_c, and the second is the resulting pseudo-orbital spanned by the plane wave basis set. The former ensures that the pseudo-orbital outside R_c experiences the correct potential from the inside of R_c. Thus, the integrated pseudo-orbital density inside R_c is not critical because it is complemented by the residual local potential and projection operators, which ensure proper resulting properties outside R_c. This way, the job of the plane wave basis set is greatly simplified

as compared to the norm-conserving pseudopotentials, i.e. because the details inside R_c are taken care of by an auxiliary set of local function.

Chapter 5

Modelling considerations

The purpose of this study is to build an understanding of water oxidation of zirconium by deconstructing the corrosion phenomenon into computationally accessible and at the same time experimentally relevant quantum chemical modules. Although converged numbers are provided, the objective is not the numbers per se but rather to gain conceptual insight by means of first-principles calculations. The adopted strategy is to identify central mini-processes which jointly close the electrochemical corrosion circuit. Density Functional Theory, DFT, is used on different models to study specific parts in the corrosion process. When modelling, there is always a tradeoff between getting fast results and good enough convergece.

The model systems used on the study are presented in the following sections along with computational details and discussion of the impact of the functional on the results.

5.1 Grain boundary model

In order to study the transition meta (TM) dependence of HPUF, see Fig. 3.2 [79, 80], a grain boundary model decorated with TM is constructed with the support of the findings by Sundell et al. They report of Ni and Fe decorated sub-grain boundaries in Zircaloy-2 [52]. This model consists of a periodically repeating hydroxylated inner interface embedded in ZrO_2 in order to model a hydroxylated grain boundary, see Fig. 5.1. A detailed description of the construction of the model is found in Paper I-Paper III. Location of the transition metal is originally

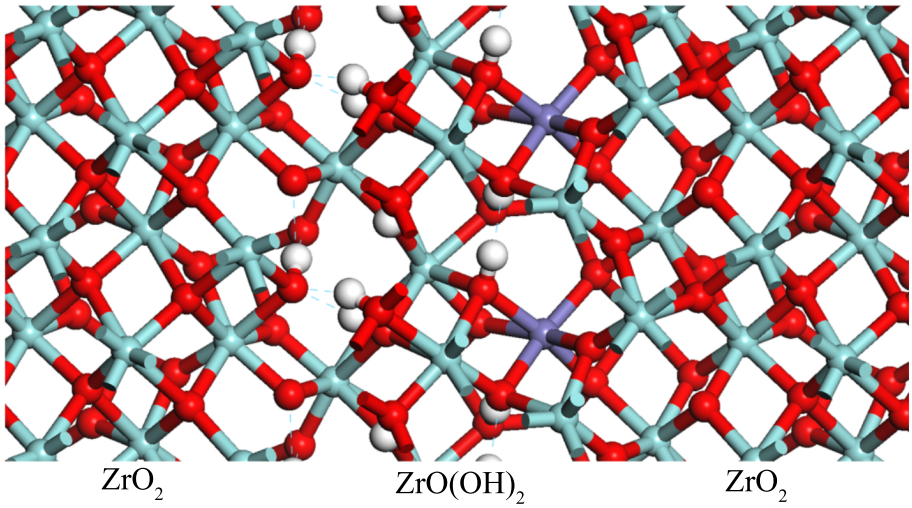

Figure 5.1: *Hydroxylated inner interface embedded in ZrO_2 to model a hydroxylated grffain boundary. Oxygen is represented as red, zirconium as light blue, hydrogen as white and iron as purple.*

at the middle of the $ZrO(OH)_2$ phase but during the following geometry optimizations the TM position is shifted to the $ZrO(OH)_2/ZrO_2$ interface. The choice of grain boundary model is far from unique. However, there are certain requirements that need to be satisfied for the model to offer a valid chemical representation of the hydroxylated interface between two ZrO_2 grains, i.e. reproducing the large band gap signature of the undoped material and a proton conducting interface. Essential to the modelling is a sufficiently flexible yet cost efficient supercell.

5.2 Oxygen dissolution in α-Zr

To study oxygen dissolution in α-Zr, oxygen atoms is placed in interstitial sites in the α-Zr matrix. Oxygen atoms in the Zr matrix energetically prefer interstitial sites over substitutional sites. There are two types of interstitial sites in the Zr matrix, octahedral sites and tetrahedral sites. Both octahedral and tetrahedral sites are tested and it is found that octahedral sites are energetically favorable. This study is based on inserted oxygen atoms in both Zr_8 and Zr_{16} super-cells. Some typical structures are displayed in Fig. 5.2. All possible permutations of putting between one and eight oxygen atoms in the eight octahedral interstitial sites in the Zr_8 structure are tested. Rotational and reflection symmetry are assumed as

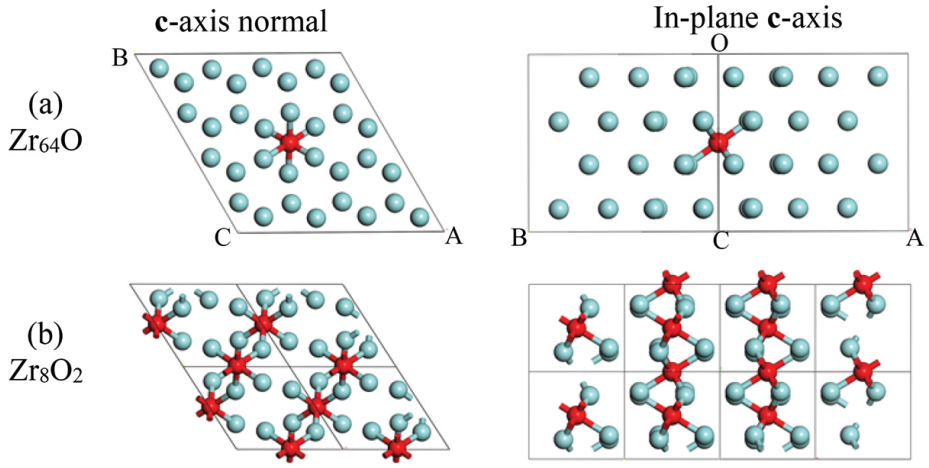

Figure 5.2: *Optimized zirconium structures with dissolved oxygen for oxygen concentrations 1.5 at.% O and 20 at.% O for (a) and (b), respectively. The structure in (a) display a Zr_6O octahedral site and the structure in (b) display chains of edge-sharing octahedra.*

well as that the two planes of interstitial sites are identical. The sampling procedure is find in Paper IV. Oxygen concentrations higher than 50 at.% are achieved by adding oxygen atoms in tetrahedral interstitial sites. One $Zr_{64}O$ structure is included to address the low oxygen concentration limit. Connection to the high-concentration limit is made through the heat of formation of Zr metal to form monocline ZrO_2. The reactivity of Zr to form ZrO_2 by means of H_2O is found to be 0.39 eV/H_2O too small, i.e. 2.72 eV compared to 3.11 eV [108]. In order to further assess the findings produced by the PBE GGA functional, comparisons are provided for some structures by means of the PBE0 hybrid functional [109], see Section 5.6.

5.3 Oxygen vacancies in bulk zirconia

Decisive for diffusion rate in bulk zirconia is the highest activation barrier for transition between two oxygen positions in the diffusional path. To examine activation barriers, the vacancy positions in Fig. 5.3 are used for monoclinic and tetragonal zirconia in (a) and (c), respectively. In both cases, an arbitrary oxygen atom in the center of the unit cells is chosen and the closest oxygen atoms around the central atoms are chosen to examine the diffusion between these positions. In the monoclinic case, all oxygen atoms at a distance of max 3 Å are included and

an extra atom at a longer distance is also included to show the effect of distance. The crystal structure in the tetragonal oxide show a higher degree of translation symmetry. All unique pathways are considered and all longer pathways can be divided in to sub-paths that are equivalent with the two shortest paths (path 1 and path 2).

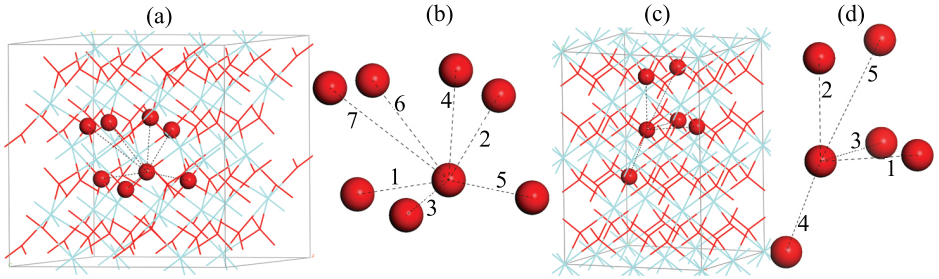

Figure 5.3: *(a): Initial atomic structure for the m$-ZrO_{2-\delta}$ calculations where the positions of oxygen vacancies are marked with red spheres. The unit cell consist of 32 oxygen atoms and 64 zirconium atoms. Light blue represents zirconium and red represents oxygen. (b): Close-up of vacancy positions in (a) with diffusion pathways marked with 1-7. (c): Initial atomic structure fro the t$-ZrO_{2-\delta}$ calculations where the positions of oxygen vacancies are marked with red spheres. The unit cell consist of 16 oxygen atoms and 32 zirconium atoms. Light blue represents zirconium and red represents oxygen. (d): Close-up of vacancy positions in (c) with diffusion pathways marked with 1-5.*

To quantify the interaction between neutral vacancies, structures with vacancies as far apart as possible in the used supercell are compared to structures where the vacancies are nucleated. Figure 5.4 show the structures used for two and four vacancies. Periodic supercells are utilized to capture signatures of individual oxygen vacancies, as well as connected dimers, trimers, and also infinite chains of connected oxygen vacancies. Consecutive energy changes upon rearrangement of oxygen vacancies are explored.

5.4 Oxide/metal interface model

A periodically repeating interface between t$-ZrO_2$ and $\alpha-$Zr is used to study properties of the oxide/metal interface. While to some extent ambiguous, it is designed to satisfy approximate epitaxy by matching the 100 plane of t$-ZrO_2$ to the 010 plane of $\alpha-$Zr. The resulting supercell, consisting of 120 atoms, is geometry optimized including optimization of the lattice parameters, see Fig.

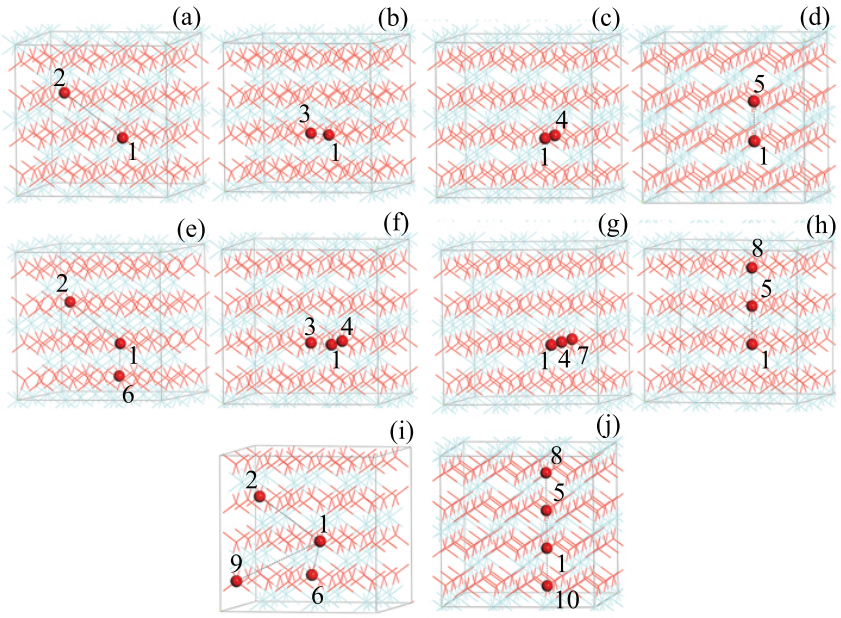

Figure 5.4: *(a-d): Four structures with two oxygen vacancies. Positions of the oxygen vacancies are indicated with red spheres. The vacancies in (a) are far apart while the vacancies in (b), (c) and (d) are adjacent. (e-h): Four structures with three oxygen vacancies. Positions of the oxygen vacancies are indicated with red spheres. The vacancies in (e) are far apart while the vacancies in (f), (g) and (h) are adjacent. (i-j): Two structures with four oxygen vacancies. The vacancies in structure (i) are far apart while the vacancies in (j) are adjacent. The structures in (d), (h) and (j) result in coalescing orbitals.*

5.5. Lattice parameters are held constant in subsequent calculations. Neutral oxygen vacancies are created by moving one oxygen atom from the oxide to an interstitial position in the $\alpha-$Zr matrix. The lattice parameters are kept constant in order to determine lower bounds to the oxygen dissolution. Vacancy positions are indicated in Fig. 5.5. The interstitial oxygen in the Zr matrix is positioned at the interface in order to capture the instantaneous local drive for dissolution.

5.5 Computational details

Throughout this study, conceptual insight is sought by means of first-principles calculations using density functional theory (DFT) [15, 16]. In the majority of all calculations the Perdue, Burke, Erntzerhof generalized gradient approxima-

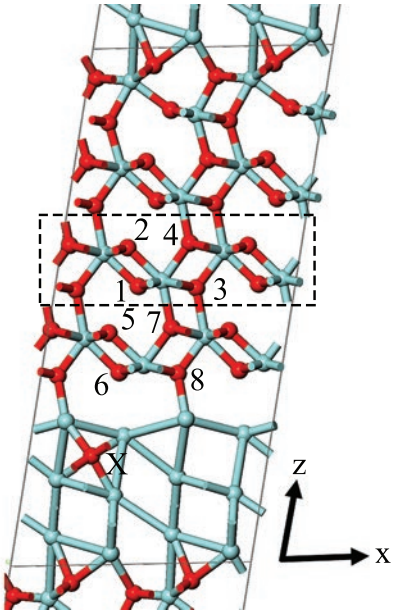

Figure 5.5: *Supercell model of metal/oxide interface where an oxygen vacancy is created in the oxide by moving one oxygen atom to the metal. The numbers 1-8 indicate the positions where oxygen vacancies are created. The position of the oxygen atom in the metal is indicated with X. Red balls refer to oxygen and light blue to zirconium.*

tion [93], i.e. PBE GGA functional, as implemented in the DMol^3 engine [107, 110] or in the CASTEP program package [111] in the Material Studios program package [112]. The difference between DMol^3 and CASTEP is that DMol^3 uses numerical basis set and CASTEP uses plane wave basis set to span the basis, see Section 4.5. In all calculations, the brillouin zone is sampled by means of the Monkhorst-Pack scheme [113], which is also checked for convergence. All transition state calculations employ the Linear/Quadratic Synchronous Transit method [114] to find activation barriers.

Calculations on the hydroxylated grain boundary model in Section 5.1 are done with DMol^3. This is used since numerical basis sets are better to deal with calculations of amorphous structures. To reduce the computational effort, inert electrons are described effectively by means of a norm-conserving pseudopotential called DFT Semi-core Pseudopotential DSPP [115]. Zero-point corrected free energy is compared with uncorrected energy and the differences are deemed negligible. The entropy contributions to reactant and product are found to cancel.

This is because the large entropy contribution commonly assigned to molecular H_2 becomes negligible at the confining grain boundary. Further details is found in Paper I-Paper III.

All calculations in Section 5.2-5.4 are made with CASTEP. The majority of these structures have a very well defined crystal structure that are good to model with plane wave basis set. In case of the oxide/metal interface calculations, CASTEP is used in order to compare these results with the results from the bulk calculations directly. The first choice to describe core electrons with CASTEP is by ultra-soft pseudo-potentials [116]. The data presented in Paper V and Paper VII are calculated with the norm-conserving pseudopotential due to convergence problems with some structures with the ultra-soft pseudopotential. For the norm-conserving pseudopotential a cut-off energy of 750 eV is used compared to 340 eV cut-off energy for the ultra-soft pseudopotential for the interface calculations in Paper VI.

Zirconium is a large band-gap isolator and have an experimental measured optical energy band gap of 5.16 eV [117]. DFT calculations with the GGA PBE underestimate the band gap, see Sec. 5.6. Some calculations are done with the PBE0 functional to validate the effect on choice of functional, see Paper IV and Paper VII. Then a norm-conserving pseudopotential [118] is used in conjunction with a 750 eV cut-off energy.

5.6 Effect of functional: GGA-PBE vs PBE0

There are no functional that gives correct values on chemical bindings and all physical constants. The main functional used in this study is the PBE GGA functional that underestimate the band gap of zirconia. In most cases this is no problem when examine energy differences between two structures. But it can be problematic if impurity states are introduced in the band gap close to the conduction band or even in the conduction band. Then this interaction between impurity states and the conduction band can be artificial. Test of the validity of the GGA PBE functional is achieved by doing calculations for some structures with the PBE0 functional. When compairing energy differences for the structures and these two completely different functionals quantitatively gives the same result. This indicates that there are the true properties of the structures are captured by the calculations.

In Fig. 5.6, the effect of the PBE0 functional is presented for m$-ZrO_2$, t$-ZrO_2$ and a transition state geometry for oxygen vacancy diffusion in t$-ZrO_2$. The band gap for m$-ZrO_2$ is calculated to 5.5 eV with PBE0 and 3.2 eV with PBE GGA, and for t$-ZrO_2$ the band gap is calculated to 5.3 eV with PBE0 and 3.2 eV with PBE GGA.

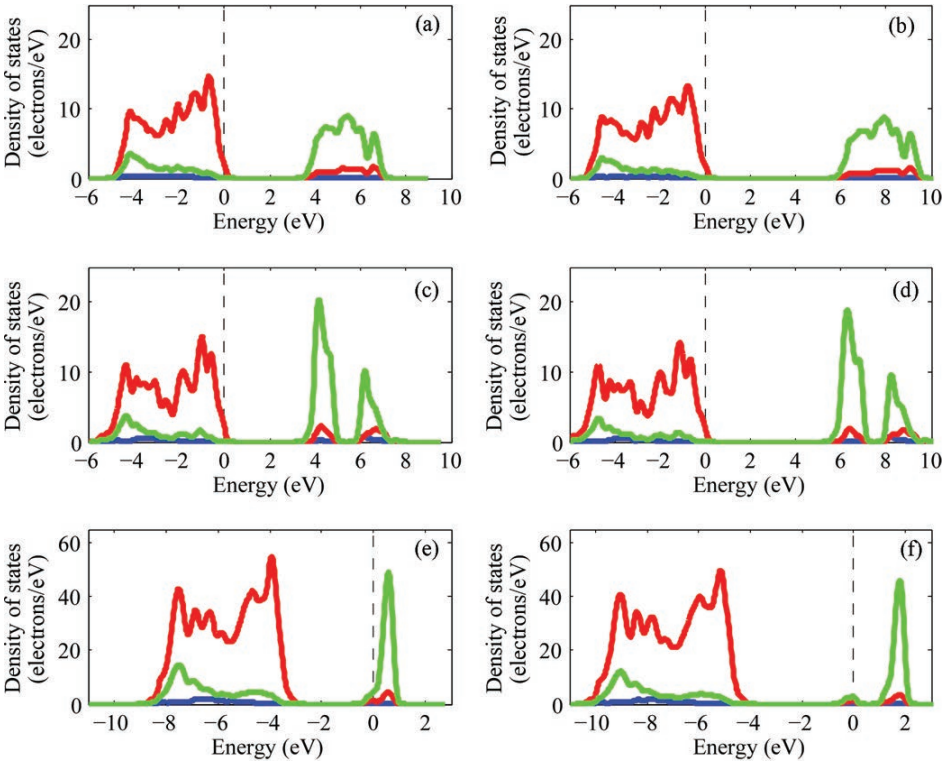

Figure 5.6: *Comparison of the effect of functional on the partial density of states for three different structures. Red represent p-states mainly consisting of oxygen states, green represent d-states mainly consisting of zirconium states and blue represent s-states. (a-b): Monoclinic Zr_4O_8 structure calculated with the GGA-PBE functional and the PBE0 functional in (a) and (b), respectively. (c-d): Tetragonal Zr_4O_8 structure calculated with the GGA-PBE functional and the PBE0 functional in (c) and (d), respectively. (e-f): Transition state structure for oxygen vacancy diffusion between position 1 and 3 in Fig. 5.3.d calculated with the GGA-PBE functional and the PBE0 functional in (e) and (f), respectively.*

In Paper V, activation barriers for oxygen vacancy diffusion is calculated for

both monoclinic and tetragonal structures. For some transition state structures the oxygen vacancy state ended up in contact to the conduction band. To examine if this interaction is true or just a result of the underestimation of the band gap with the GGA PBE functional, a PBE0 calculation is done for one of these structures. The difference in partial density of states is shown in Fig. 5.6.e and 5.6.f, and a separation between the vacancy state and the conduction band is introduced with PBE0. The activation barrier for the transition state geometry is changed from 1.1 eV calculated with PBE GGA functional to 1.5 eV calculated with PBE0 functional.

Figure 5.7 show the energetics of formation of dissolved oxygen structures from ZrO_2 and Zr according to

$$\frac{1}{2}ZrO_2 + \left(x - \frac{1}{2}\right)Zr \rightarrow Zr_xO. \tag{5.1}$$

To validate the energy minimum in the figure all structures with the Zr_8-supercell are calculated with the PBE0 functional, for details see Paper IV. The energy minimum is also present with the PBE0 calculations and this data show a similar or increased stability.

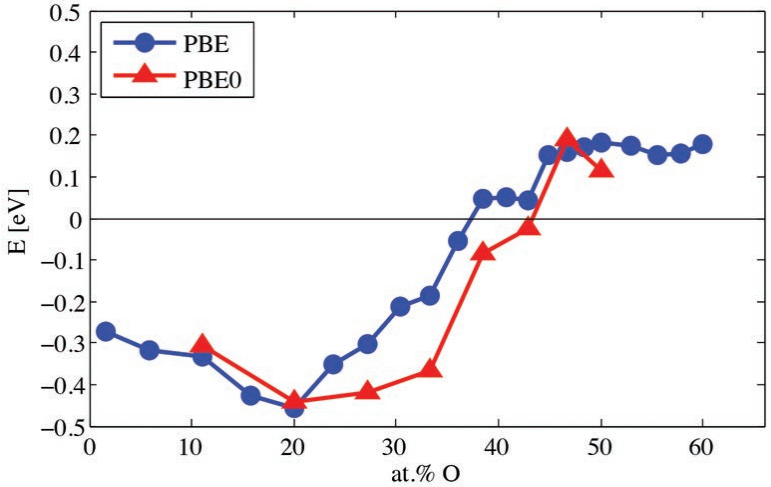

Figure 5.7: *The energetics of formation of dissolved oxygen structures from ZrO_2 and Zr according to reaction 5.1 for the most stable structures calculated with the GGA PBE functional in blue. All structures with the Zr_8-supercell are calculated with the PBE0 functional (in red) to validate the energy minimum.*

In Paper VII we study the oxygen vacancy nucleation. A large repulsion along with a vacancy state just below the conduction band is introduced when two vacancies nucleate in the *c*-direction, see Fig. 5.8. The energy difference of the structure in Fig. 5.4.d relative to the structure in Fig. 5.4.a is 5.4 eV and this value is changed to 6.5 eV when calculated with the PBE0 functional. As a reference, the energy difference of the structure in Fig. 5.4.b relative to the structure in Fig. 5.4.a is 0.03 eV and this value is changed to 0.01 eV calculated with the PBE0 functional. A comparison of the impact on the density of states upon including exact exchange by the PBE0 functional for the structures displayed in Fig. 5.4.a, 5.4.d and 5.4.f is summarized in Fig. 5.8.

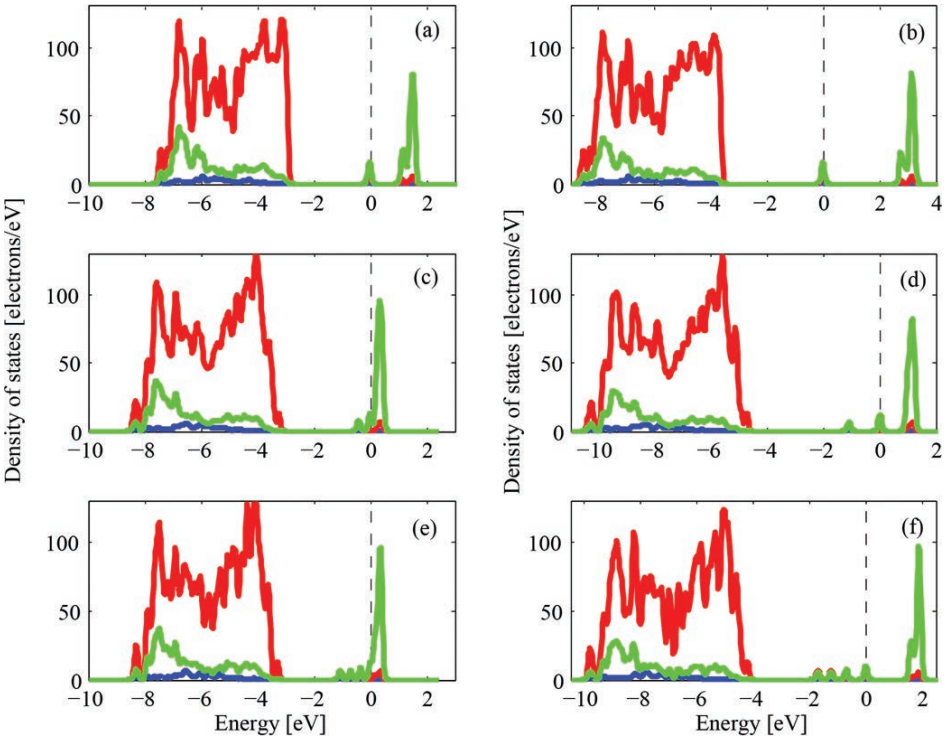

Figure 5.8: *Impact of choice of functional on density of states DOS and band gap. GGA-PBE (left panel) and PBE0 (right panel) are compared. (a): GGA-PBE DOS for the structure in Fig. 5.4.a with two vacancies separated in space. (b): As in (a) with the PBE0 functional. (c): GGA-PBE DOS for the structure in 5.4.d with two vacancies next to each other. (d): As in (c) with the PBE0 functional. (e): GGA-PBE DOS for the structure in 5.4.j with four vacancies next to each other. (f): As in (e) with the PBE0 functional.*

In order to validate that the impurity states in Fig. 5.8.e indeed includes a Rydberg-like quasi-delocalized state, which is not an artifact of the self-interaction error in GGA-PBE underestimating the band gap, the PBE0 hybrid functional is resorted to. While the impurity states become clearly separated from the conduction band, compare Fig. 5.8.e and 5.8.f, still the delocalized character remains, see Fig. 5.9.d. The two highest occupied Kohn-Sham states for the structures in Fig. 5.4.a and Fig. 5.4.d calculated with PBE0 are presented in Fig. 5.9. It is noted how delocalization of the highest occupied KS-state is favored somewhat unexpectedly in spite of PBE0 partly correcting for self-interaction error. In contrast, the difference in character of the highest KS-state, whether computed with GGA-PBE or PBE0 for the structure in Fig. 5.4.j, comes out clearly in Fig. 5.9. It is a result of PBE0 suppressing the self-interaction error in GGA-PBE, which also underestimate the band gap in case of the latter.

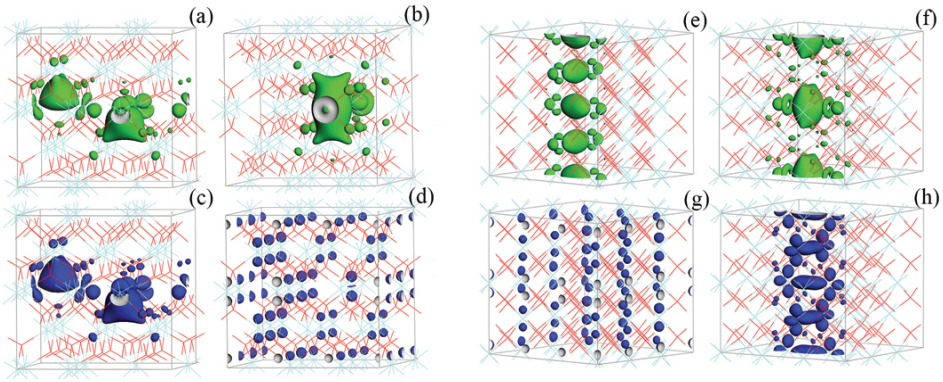

Figure 5.9: *(a-d): Second-highest KS-state (a) and highest KS-state (c) for the structures in Fig. 5.4.a calculated with the PBE0 functional (corresponding DOS in Fig. 5.8.b). Second-highest KS-state (b) and highest KS-state (d) for the structures in Fig. 5.4.d calculated with the PBE0 functional (corresponding DOS in Fig. 5.8.d). Note how delocalization is favored in spite of PBE0 partly correcting for self-interaction error. (e-h): Second-highest KS-state (e) and highest KS-state (g) for the structure in Fig. 5.4.j calculated with the GGA-PBE functional (corresponding DOS in Fig. 5.8.e). Second-highest KS-state (f) and highest KS-state (h) for the structure in Fig. 5.4.j calculated with the PBE0 functional (corresponding DOS in Fig. 5.8.f). Note impact of self-interaction error to favor delocalization.*

Chapter 6

Result and discussion

This thesis is based on seven papers all covering different parts of zirconium oxidation by water. The main focus of this study is to find key processes that determine the complex oxidation of zirconium alloys in order to understand mechanism behind the unwanted hydrogen pick-up phenomena. Rather than the final answer, this work seek an internally consistent working hypothesis. In doing so, empirical observations are complemented by corresponding first principles calculations. The viewpoint is from an electrochemical perspective where anode and cathode are localized and separated in space. Anode and cathode reactions are identified as well as reactions forming these. The transport of electrons and oxygen ions is also addressed. The electro neutrality of the system is crusial even though small instantaneous charge separations are introduced.

In this chapter a brief summary of the main results of the papers are presented. A presentation of the working hypothesis for oxidation of zirconium alloys by water is given. This is followed by a more detailed presentation of the results and discussions that the hypothesis is based upon. Finally, the fate of hydrogen and its impact in the oxidation process is summarized.

6.1 Summary of papers

Paper I *Toward a Comprehensive Mechanistic Understanding of Hydrogen Uptake in Zirconium Alloys by Combining Atom Probe Analysis With Electronic Structure Calculations:* This paper consists of three parts. First the cathode is studied and later the anode. Both these studies are fur-

ther analyzed in later publications. For the cathode study, a hydroxylated grain boundary model decorated with TM is used, see Fig. 5.1, where a three-center hydride ion ($TM-H^{-}-Zr$) is identified. It also present electronic characterization of hydride ion and vibration frequency for some hydride ion species. The vibration frequencies are found to be distinct from frequencies of protons in hydroxide. Hydrogen evolution reaction from proton-hydride ion recombination is identified, and we found a correlation between energetics of proton-hydride ion recombination and HPUF. In the second part of the study we gain insights into electronic and chemical properties of $Zr(O_x)/ZrO_2$ interface. Drive for ZrO_2 dissolution and simultaneous hydrogen absorption in zirconium matrix is presented. Hydrogen associated vibration frequency of $H_xZr(O_y)$ are calculated and found to be separated from both hydroxides and hydride ion species. Third part of the paper covers substitutional doping of Nb in $m-ZrO_2$. Electronic characteristics show that Nb states are located close to the conduction band and offers states in the band gap offering easier transport of electrons.

Paper II *Impact of Additives on Zirconium Oxidation by Water: Mechanistic Insights from First Principles:* A continuation of Paper I and the model in Fig. 5.1 is used again to further study the cathode reaction. The analysis of the three-center hydride ion species ($TM-H^{-}-Zr$) continues with focus on the origin of TM dependence on proton-hydride ion recombination reaction energy. Crucial for energetics of HER is change in coordination of transition metal ions upon release of H_2 into the grain boundary, i.e. hydride ion coordination in reactant and oxide ion in product. Understanding of energetics is made by considered ligand field theory and occupation of e_g^*. Structural support for proton-hydride ion recombination reaction are presented and properties of H_2 intermediates are identified.

Paper III *Confinement Dependence of Electro-Catalysts for Hydrogen Evolution from Water Splitting:* A continuation of Paper I and Paper II. Once again, the model in Fig. 5.1 is used. This time it is used to articulate a particular generic deconstruction of the electrode/electro-catalyst assembly for the cathode process during water splitting. The concept of confinement effect is introduced where the environment of the H_2 molecule affect the energy of the molecule. A computational strategy is developed to select an electro-catalyst for hydrogen evolution, where the choice of TM catalyst is guided by the confining environment. The list of tested TM is expanded with Pd, Ag, Pt and Au. The present approach offers a complementary

computational strategy to rank catalysts for HER from water splitting.

Paper IV *On the Fate of Hydrogen during Zirconium Oxidation by Water: Effect of oxygen dissolution in α-Zr:* Oxygen concentration dependence of anode potential is studied and is a continuation of the anode study in Paper I. Impact of oxygen concentration on co-absorption of hydrogen in Zr is examined and found to be independent for oxygen-zirconium ratios up to 1:1. Experimental solubility limit for oxygen in α-Zr is semi-quantitatively reproduced and the gradually buildup of bandgap in DOS from Zr_8 to Zr_8O_{16} is presented. This is used to examine how solubility of oxygen affects the corrosion properties. It was found that at oxygen concentrations of ~ 30 at.% there are configurations where the anode potential is not able to for all hydride ions studied in Paper I-III. A difference in activation barrier for diffusion of oxygen in α-Zr depending of phase direction is reported.

Paper V *Oxidation of Zr Alloys by Water - Theory from First Principles:* Transport of oxygen vacancies and electrons from anode to cathode is studied and used to formulate a theory to describe oxide growth on zirconium alloys in contact with water. A polycrystalline duplex barrier oxide composed of submicron t$-ZrO_2$ and m$-ZrO_2$ is considered. We modify Wagner theory and Tedmon kinetics to include effects of oxide scale charging and present a novel sub-parabolic rate equation. Actual charging upon formation of charged vacancies is included in the activation energy for oxygen vacancy diffusion. We also calculate bulk activation energies for oxygen vacancy diffusion. Activation energies are dependent of charge of the vacancy. Lower barriers are found in t$-ZrO_2$ compared to m$-ZrO_2$, especially for charged vacancies. An oxidation theory is introduced with two parallel channels. One according to classical Wagner theory with transport of charged oxygen vacancies and one channel where neutral vacancies are transported by concentration driven diffusion according Fick. First, the Wagnerian channel is dominating but it becomes suppressed as the oxide grows. The Fickian channel becomes more and more pronounced at the same time and the concentration of neutral oxygen vacancies with slow transport through the oxide increases. We proposed that the coalescence of neutral oxygen vacancies resulting in pores to offer easy electron paths and short-circuiting of anode and cathode and opens a hydrogen pick-up channel.

Paper VI *Oxygen Vacancy Formation, Mobility and Hydrogen Pick-up during Oxidation of Zirconium by Water:* The present paper is focusing on the ef-

fective anode and a metal/oxide interface model is used to study this. The concept of "proto-anode" is introduced, saying that the oxygen dissolution is the set up for the anode reaction that is set to be the actual charging of the vacancy. Enthalpies of formation of oxygen vacancy at the metal/oxide interface are presented and compared to those in bulk. The arbitrary interface model is used to get a consistency check of the bulk calculations from Paper I and Paper V. Insights of the local structure of an amorphous metal/oxide interface is presented.

Paper VII *Possible Origin and Roles of Nano-porosity in ZrO_2 Scales for Hydrogen Pick-up in Zr Alloys:* This paper is a continuation of Paper V. The drive for nucleation of neutral oxygen vacancies is examined. Hydrogen was found to assist vacancy nucleation and a mechanism for hydrogen assisted build-up of nano-porosity was proposed. The activation barrier for hydrogen transfer between two V_O positions is calculated and conditions for hydrogen permeation through the barrier oxide by cooperating in pore formation is explored.

6.2 Oxidation of zirconium by water - working hypothesis

To model the complex oxide layer a polycrystalline duplex barrier oxide is considered, see Fig. 6.1. The barrier oxide is assumed to consist of a tetragonal dominating layer at the oxide/metal interface. The monoclinic phase is dominating further away from the interface. Above the barrier oxide, there is a non-barrier oxide with large cracks where water transport is unlimited. The interface of the non-barrier/barrier oxide is here seen as the water/oxide interface. This model with a layer rich with tetragonal phase is inspired by recent findings by Garner et al. [119]. They state that the tetragonal fraction identified in focused ion beam (FIB) samples are much lower compared to non-destructive measurements like X-ray diffraction (XRD). They propose that there are tetragonal grains with a favorably orientation that grows above critical size and are only stable in the presence of stress in the oxide. Grains that are not favorably oriented remain small enough so that size stabilize the grains even when most of the compressive stress in the oxide is relieved. Garner et al. also report of a large fraction of twin boundaries in the oxide and argue that the majority of the monoclinic grains originates from transformed tetragonal grains.

We propose that two channels contribute to the oxidation process, one according

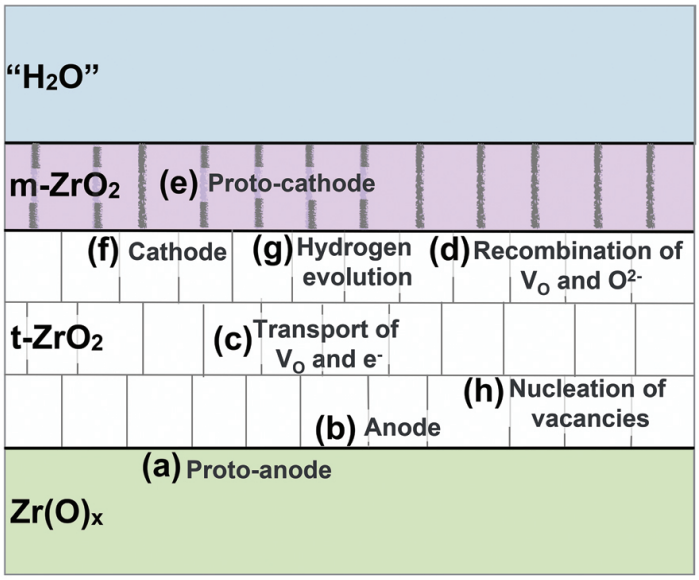

Figure 6.1: *Schematic representation of the oxide barrier layer and where the key processes involved in the working hypothesis take place. The oxide layer is considered to be composed of a complex polycrystalline duplex barrier oxide of $m-ZrO_2$ and $t-ZrO_2$ under a non-barrier oxide transparent to water here represented by "H_2O". Beneath the oxide layer is a metal layer with dissolved oxygen atoms represented by $Zr(O)_x$*

to classical oxidation theory involving hydrogen evolution at the effective cathode (see Fig. 6.1f), and one which allows inwards transport of protons against the electric field, i.e., hydrogen pick-up. The two channels are associated with charged $V_O{}^{q+}$ and uncharged oxygen vacancy V_O formations at the metal/oxide interface. The first channel, i.e., classical oxidation theory, is summarized in Fig. 6.1a-g. The barrier oxide of zirconia is taken to be subdivided into a defect-rich tetragonal phase providing both electron and ion conductivity, and a defect-free monoclinic phase permeating water in the form of hydroxides resulting from the hydrolysis products of O^{2-} and H_2O. The cathode process, occurring at the interface between tetragonal and monoclinic phases, comprised hydrogen evolution in conjunction with recombination of charged oxygen vacancies in the tetragonal phase and oxygen ions. The second channel give rise to hydrogen pick-up. According to the theory developed in Paper V, the formation of new charged vacancies becomes more and more demanding due to charging of the oxide scale. The result is an increasing concnetration of neutral vacancies as the oxide thickens and a slower oxidation process due to higher activation barrier for diffusion

of neutral vacancies. At a high neutral vacancy concentration these can start to nucleate (Fig 6.1.h). Hydrogen or hydride ions can catalyze nucleation of vacancies in a direction where coherent vacancy pathways offers hydrogen diffusion through the barrier oxide with low barriers for diffusion. This allows for a fast hydrogen pick-up.

Location of main reactions in the oxidation process are summarized in Fig. 6.1 and these reactions are described by:

(a) Anode forming reaction is assigned to dissolution of oxygen in the zirconium matrix, i.e. the "proto-anode". A neutral oxygen atom from an oxygen ion in the oxide at the oxide/metal interface is incorporated in $Zr(O)_x$. The oxygen concentration in the Zr matrix is increased and a vacancy is created in the oxide. The vacancy is neutral, i.e. there are two electrons associated with the vacancy so the surrounding oxide matrix is unaffected with no change in charge.

(b) Separation of electrons from the neutral oxygen vacancy forming a charged vacancy is assigned the anode reaction,

$$V_O \rightarrow {V_O}^{q+} + qe^-, \quad q = \{1,2\}. \tag{6.1}$$

(c) Coexistence of charged and neutral vacancies through the oxide offers peculating electron diffusion paths through the barrier oxide. In the $t-ZrO_2$ layer the activation barrier for vacancy diffusion of charged vacancies is very low. By assuming that the transport of electrons and vacancies through the tetragonal oxide layer is much faster than the transport of water through the barrier oxide, we get the location of the cathode process will be at the monoclinic/tetragonal interface. As long as a large fraction of vacancies are charged the oxidation process is fast where both electrons and oxygen vacancies can easily be transported from the anode to the cathode.

(d) The vacancies are recombined with oxide ions from hydroxide originating from the transported water,

$${V_O}^{2+} + O^{2+} \rightarrow \emptyset \tag{6.2}$$

where $\emptyset$ represents that an ion and a vacancy is recombined and oxide is formed.

(e) The proto-cathode is here said to be the hydroxylation of grain boundaries that offers transport of protons in form of hydroxides to the location of the cathode process.

(f) The cathode reaction is the formation of the hydride ion, i.e. the reduction of a proton,

$$\mathrm{H}^{+} + 2\mathrm{e}^{-} \rightarrow \mathrm{H}^{-} \tag{6.3}$$

or

$$\mathrm{TM}_{\mathrm{GB}}^{+\mathrm{x}} \cdots \mathrm{Zr}^{+\mathrm{IV}} + OH^{-} + V_{O}^{2-} \rightarrow TM_{GB}^{+\mathrm{x}} - H^{-} - Zr^{+IV} + \emptyset. \tag{6.4}$$

(g) This can be followed by a proton-hydride ion recombination step identified as

$$\mathrm{OH}^{-} + \mathrm{TM}_{\mathrm{GB}}^{+\mathrm{x}} - \mathrm{H}^{-} - \mathrm{Zr}^{+\mathrm{IV}} \rightarrow \mathrm{O}^{2-} + \mathrm{TM}_{\mathrm{GB}}^{+\mathrm{x}} + [\mathrm{H}_2]_{\mathrm{GB}} + \mathrm{Zr}^{+\mathrm{IV}}, \tag{6.5}$$

where $[\mathrm{H}_2]_{\mathrm{GB}}$ represents H_2 in grain boundary.

(h) At a sufficient high concentration of neutral vacancies these can start to nucleate.

A more detailed description of the key processes of the working hypothesis along with computational results supporting them are found in the coming sections.

6.3 Anode reaction

Charging of neutral oxygen vacancy is set to be the anode reaction, see Eq. 6.1. The original neutrality of the vacancy can be seen in Fig. 6.2a where highest occupied Kohn-Sham orbital display a local origin of the vacancy associated electrons. Fig. 6.2b-c show the difference in partial density of states for a neutral and 2+ charged vacancy in (b) and (c), respectively. The anode forming reaction, i.e. proto-anode, is assigned to the dissolution of oxygen in the zirconium matrix. The solubility limit of $\mathrm{m}-\mathrm{ZrO}_2$ is reported to 29 at.% [28]. This is semi-quantitative reproduced in Paper IV where insights into electronic and chemical properties of $\mathrm{Zr}(\mathrm{O}_\mathrm{x})/\mathrm{ZrO}_2$ interface is gained. A drive for ZrO_2 dissolution in α-Zr is obtained for concentrations up to 33 at.%, see Fig. 5.7. There is a difference in activation barrier for diffusion of oxygen in α-Zr depending of phase direction. The activation energy for interstitial oxygen diffusion in the Zr matrix comes out 4 times higher in the c-direction. This implies that the formation of V_O is not the

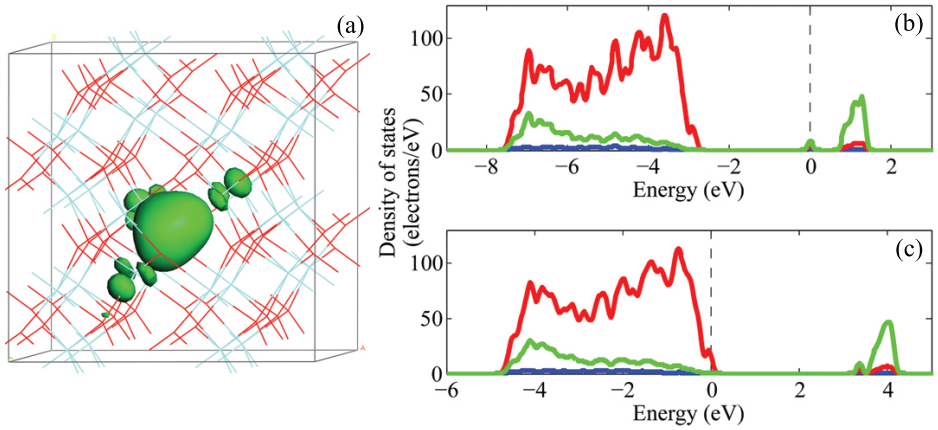

Figure 6.2: *(a): Localized electrons at the oxygen vacancy showing a neutral vacancy. The surrounding matrix experiences the same charge as before the oxygen atom was removed. (b): Density of states (DOS) for m−$Zr_{32}O_{63}$ with a neutral vacancy. (c): DOS for the same geometry as in (b) but with a 2+ charged vacancy instead of neutral as in (b). The Fermi level is moved from the state associated with the vacancy as in (b) to the edge of the oxygen band as in (c) . Red is partial DOS for O 2p and green is partial DOS for Zr 4d.*

rate limiting step for the ZrO_2 dissolution process.

Enthalpy of formation of a neutral oxygen vacancy varies between -0.03 eV and -1.26 eV for the vacancy positions indicated in Fig. 5.5. The oxygen atoms are incorporated at interstitial sights in the zirconium matrix. The enthalpy variation comes from the variation in the local surrounding for the different vacancy positions. In particular the immediate interface clearly expresses the chemical incompatibility of the two phases. When comparing for example sites 6 and 8, the terminal role of the former as compared to the integrated position of the latter is taken to explain the increased stability on dissolution of oyxgen atom at site 6. It is interesting however, that already less than 1 nm into the oxide, the drive for dissolution stabilizes, cf. sites 1-4. The corresponding enthalpies of formation of neutral vacancies in bulk come out endothermic by approximately 0.5 eV in the periodic supercell calculations for both the tetragonal and monoclinic phases. This is taken to be an upper bound when bearing in mind that the barrier oxide is nano-crystalline early during barrier oxide formation, but also supports the notion of vacancy nucleation to form quasi-spherical cavities as well as pores at grain boundaries as the grains grow.

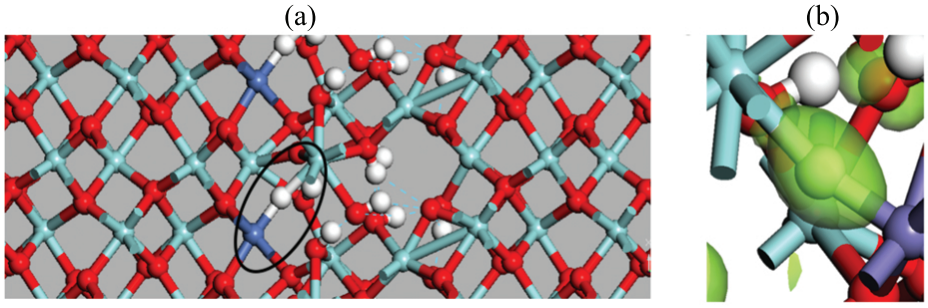

Figure 6.3: *(a): A Ni associated three-center hydride ion (encircled) in the hydroxylated intreface surrounded by bulk zirconia. (b): An electron orbital (green) with the center on the H-part in the three-centered complex, here Fe associated.*

6.4 Cathode reaction

For the cathode study, a hydroxylated grain boundary model decorated with TM is used, see Fig. 5.1, where a three-center hydride ion ($TM-H^{-}-Zr$) is identified for TM in oxidation state +II and +II, see Fig. 6.3. Partial density of states for the three center complex can be seen in Fig. 6.4b, where the states below the Fermi level for the hydrogen atom clearly tells of electrons that are associated with the hydrogen atom. The partial density of states for the whole system is displayed in Fig. 6.4a.

Oxygen concentration dependence of anode potential is studied and is used to examine how solubility of oxygen affects the corrosion properties and it was found that at oxygen concentrations of ~ 30 at.% and above there are configurations where the anode potential is not able to for all hydride ion, see Fig. 6.5.

6.5 Hydrogen evolution

Hydrogen evolution reaction from proton-hydride ion recombination is identified according to Eq. 6.5. An example of reactant and product structures are find in Fig. 6.6. Dependence of TM on the hydrogen evolution reaction as well as a correlation between energetics of proton-hydride ion recombination and HPUF is presented in Fig. 6.7. The three-center hydride ion species ($TM-H^{-}-Zr$) is continued analyzed with focus on the origin of TM dependence on proton-hydride ion recombination reaction energy. Crucial for energetics of hydrogen evolution reaction (HER) is change in coordination of transition metal ions upon release of

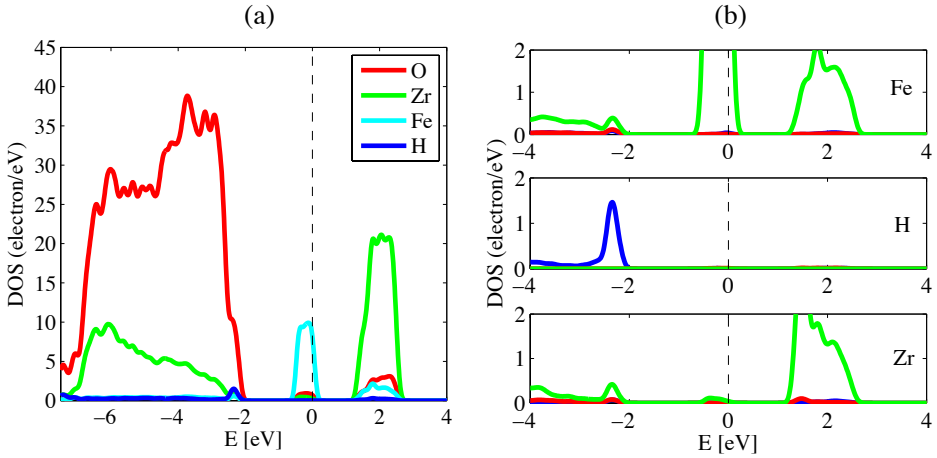

Figure 6.4: *(a): Partial density of states for Fig. 6.3.b showing the contribution form oxygen, zirconium, iron and hydrogen. (b): Partial density of states for the three atoms in the three-center hydride.*

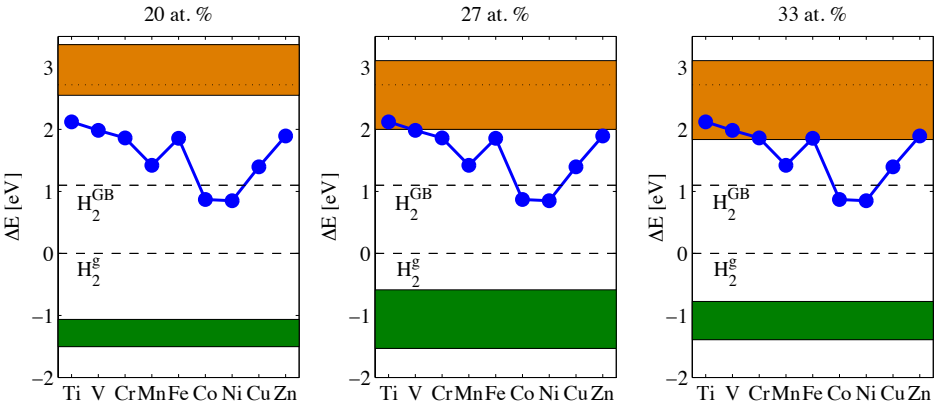

Figure 6.5: *As the oxygen concentration increases, the spread in anode potential increases. In as much as these values represent the energy required to form intermediate transition metal hydride ions, overlap between anode potentials (orange) and the additive associated curve (blue) implies inability to access the hydrogen evolution channel for those elements and potentials. Green band represent spread in dissolution of 2H in some structure with initial oxygen concentrations of 20 at.% O, 27 at.% O and 33 at.% O. Dashed line at 0 eV corresponds to $H_2(g)$ and dashed line at 1.1 eV corresponds to H_2 in a oxide grain boundary.*

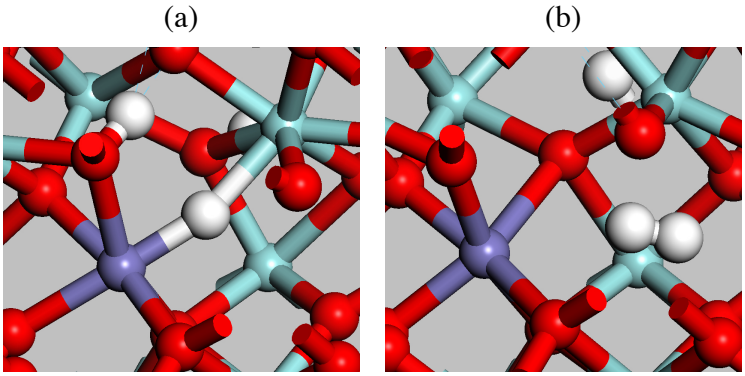

Figure 6.6: *The structure in (a) corresponds to the reactant in reaction 6.5 with the hydride ion and the proton that in (b) have formed H_2 by hydride-proton recombination. The structure in (b) corresponds to the product in reaction 6.5. The transition metals is iron in oxidation state +II.*

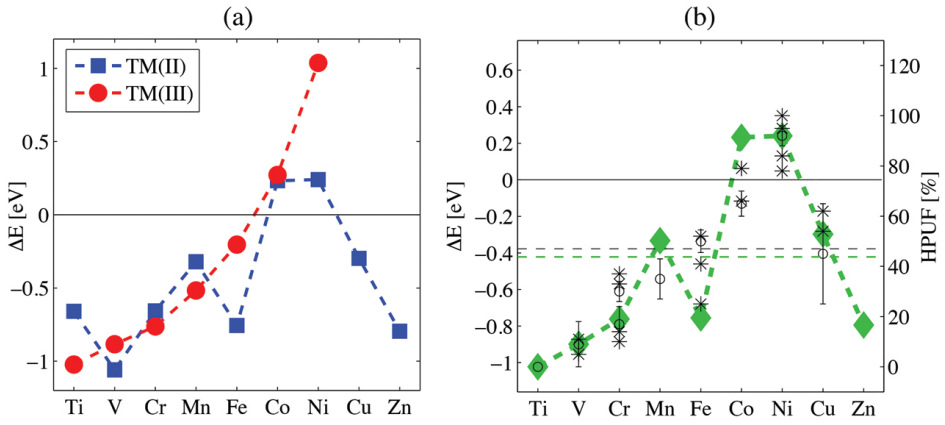

Figure 6.7: *(a): Energy gain for H_2 formation from TM hydride ion (see reaction 6.5) for TM^{+II} (squares) and TM^{+III} (dots), respectively. The hydride ions with Co or Ni are more stable than H_2 in the grain boundary. (b): The energy gain for H_2 formation have the same "vulcano" shape as experimental HPUF data; ∘ from [80] and ∗ from [79]. Lower horizontal dashed line in green corresponds to hydrogen evolution from Zr^{+IV} hydride at GB with Ca^{+II} as spectator, while the upper horizontal dashed line in black is HPUF in pure ZrO_2 from [79].*

H_2 in to the grain boundary, i.e. hydride ion coordination in reactant and oxide ion in product, see Fig. 6.8. Understanding of energetics is made by considering

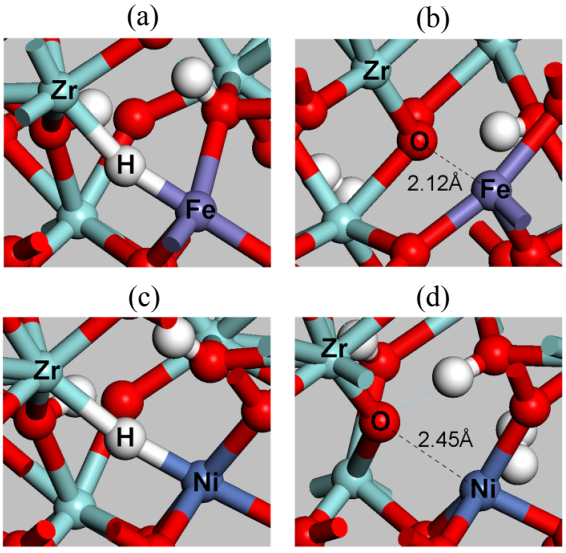

Figure 6.8: *(a) and (c) illustrate Fe and Ni associated three-center hydrides. In (b) and (d) the TM coordination to the hydride has been replaced by the coordination (dashed line) to O^{2-}. Note the difference in TM-O bond distance, 2.12 Å for Fe^{II} and 2.45 Å for Ni^{II}, which explains the smaller exothermicity associated with the HER of the latter as compared with the former (see Fig. 6.7).*

ligand field theory and occupation of e_g^*. Structural support for proton-hydride ion recombination reaction is identified by a H_2 intermediate structure. Unoccupied e_g^* orbitals on the transition metal result in incresed stability when the TM$-H^-$ bond is changed to a TM$-H_2$ bond and even more when replaced by a new $O_2{}^-$ coordination. Consequently, sensitive dependence of HER on choice of spin state is observed as different spin states cause different e_g^* occupations.

The concept of confinement effect is introduced where the environment of the H_2 molecule affect the energy of the molecule. There is a drive on 1.1 eV/H_2 to release H_2 from the containing grain boundary,

$$[H_2]_{\text{grain boundary}} \rightarrow H_2(g) + [\quad]_{\text{grain boundary}}. \tag{6.6}$$

Table 6.1: *Activation energies (eV) of oxygen vacancy diffusion at different charge for seven pathways in the* m$-ZrO_{2-\delta}$ *unit cell, see Fig. 5.3a. The diffusion distances are also presented.*

	Path 1	Path 2	Path 3	Path 4	Path 5	Path 6	Path 7
q=0	1.9	2.2	1.5	2.0	2.3	2.6	2.9
q=1	1.3	1.5	1.2	1.6	2.2	2.3	3.1
q=2	0.9	0.9	1.0	1.4	2.0	2.2	3.4
Distance (Å)	2.568	2.592	2.787	2.883	2.962	3.059	3.857

Table 6.2: *Activation energies (eV) of oxygen vacancy diffusion at different charge for five pathways in the* t$-ZrO_{2-\delta}$ *unit cell, see Fig. 5.3c. The diffusion distances are also presented.*

	Path 1	Path 2	Path 3	Path 4	Path 5
q=0	1.1	1.1	3.1	1.0	3.2
q=1	0.1	0.2	2.0	1.1	3.4
q=2	0.2	0.5	2.6	1.1	3.9
Distance (Å)	2.562	2.573	3.624	3.632	4.444

6.6 Transport of oxygen vacancies and electrons

Maintaining the ZrO_2 barrier oxide requires sufficiently high mobility of vacancies along the chemical potential gradient between anode and cathode to counter the dissolution process. Activation energies for displacement of uncharged and charged vacancies for the seven diffusion paths in Fig. 5.3a are summarized in Table 6.1 for m$-ZrO_2$. Similarly, the oxygen vacancy sites considered for t$-ZrO_2$ are displayed in Fig. 5.3c. The corresponding activation energies are found in Table 6.2. Uncharged vacancies are seen to display significantly higher diffusion barriers than their charged counterparts. This difference is indeed consistent with structural effects on the electronic density of states, that is uncharged V_O state appear in the band gap while displacement of the corresponding states to the conduction band is observed for the 2+ charged vacancy (see Fig. 6.2b-c). Moreover, the activation energies for diffusion come down substantially going from m$-ZrO_{2-\delta}$ to t$-ZrO_{2-\delta}$. Taking into consideration that the high-activation-energy paths in Table 6.2 may be broken down into alternative short low-activation energy steps, see Fig. 6.9, renders the activation energy at most 0.5 eV. Also the longer paths in m$-ZrO_2$ can be divided into shorter paths but not as effectively as for t$-ZrO_{2-\delta}$. Sensitivity to charge is investigated by addressing

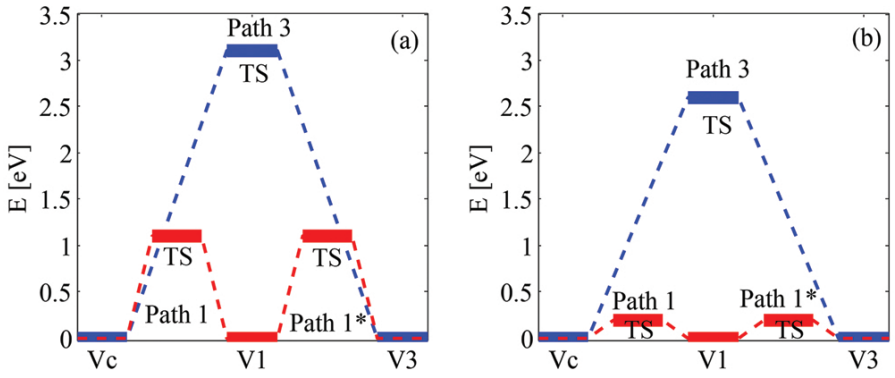

Figure 6.9: *Energy of transition state (TS) relative start structure for oxygen vacancy diffusion between two vacancy positions in* t$-ZrO_{2-\delta}$. *The longer diffusion path 3 (blue) can be devided into two steps, path 1 and path 1 equivalent, with much lower activation barriers for diffusion. (a) is for neutral vacancy and (b) is for 2+ charged vacancy. Vc is the central vacancy in Fig. 5.3b and V1 and V3 are the vacancies at the end of path 1 and 3, respectively. Path 1* denotes a path equivalent to path 1. In case of* t$-ZrO_{2-\delta}$, *all long paths (paths 3-5) can be divided into a sequences of the shorter path 1 and path 2.*

singly charged oxygen vacancies, for both m$-ZrO_{2-\delta}$ and t$-ZrO_{2-\delta}$. It is gratifying to note that singly charged vacancies display activation energies of similar magnitudes as their doubly charged counterparts. In particular, the smallness of activation energy in tetragonal phase is again highlighted. This supports the notion that homogeneous build-up of charge will impact the effective diffusivity in the t$-ZrO_{2-\delta}$ phase in a major way.

Coexistance of neutral and charged oxygen vacancies offer percolating electron diffusion paths through the barrier oxide on the states that are introduced in the band gap by the oxygen vacancy, see Fig. 6.2b-c. An other way of offer paths for electron transport is doping of the oxide with alloying elements. Substitutional doping of Nb in m$-ZrO_2$ is examined and electronic characteristics of substitutional Nb doping of ZrO_2 show that Nb states are located close to the conduction band and offer states in the band gap, see Fig. 6.10. These offers easier transport of electrons from the anode. The concentrations of Nb atoms in the oxide matrix is crusial for the electron transport properties through the oxide.

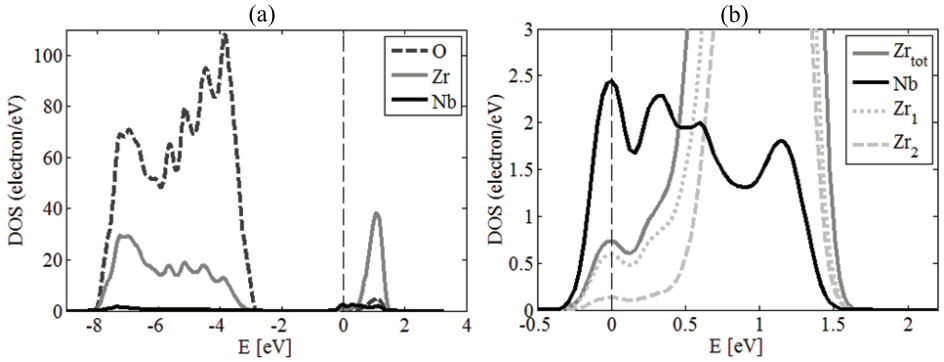

Figure 6.10: *(a) Atom resolved PDOS for Nb(IV) doped ZrO_2 showing niobium states just below the conduction band. (b) Atom resolved PDOS for Nb and Zr in Nb(IV) doped ZrO_2, where the PDOS(Zrtot) is further subdivided into contributions from Zr_1 nearest neighbors to Nb(IV) and the remaining Zr(IV) ions, comprising Zr_2.*

6.7 Nucleation of vacancies

One proposal of how hydrogen is transported through the barrier oxide to the metal is in pores in the oxide. In order to find any evidence for this theory, nucleation of neutral vacancies is examined. Figure 6.11 displays the dimerization, trimerization and tetramerization energies of the vacancies. Activation barrier for hydrogen transfer between two V_O positions is calculated and conditions for hydrogen permeation through the barrier oxide by cooperating in pore formation is explored. The barrier for hydrogen transfer between two oxygen vacancy positions depends on distance and direction of diffusion in the solid. The latter becomes particularly crucial as two adjacent vacancies may be either connected or disconnected. Activation energy for diffusion between the two V_O positions shown in Fig. 5.4d is 0.4 eV. This is in contrast to $E_A \sim 2.3$ eV for hydrogen diffusion between two adjacent V_O positions in Fig. 5.4c. The latter larger value is indeed owing to the sites being disconnected. The large barrier for creating the structure in Fig. 5.4d makes it inaccessible. To clarify the impact of single hydrogen residing in oxygen vacancies on dimerization, the stability of the structure in Fig. 5.4d is increased by adding one hydrogen atom in one of the vacancies, compare blue and green a-d data in Fig. 6.11 for two vacancies where the blue data represent dimerization without a hydrogen atom present and the green data represents dimerization with a hydrogen atom present in one of the oxygen vacancies. Clearly, hydrogen assisted dimerization is inferred.

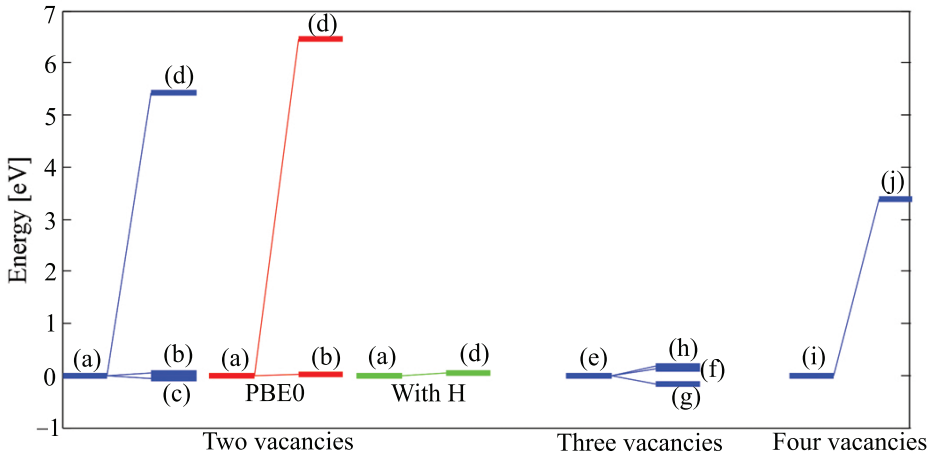

Figure 6.11: *Presented are the relative stability of structures for two, three and four vacancies. The letters corresponds to the structures in Fig. 5.4 for two, three and four vacancies, respectively. The data in red is calculated with the PBE0 hybrid functional and the data in blue are calculated with the GGA-PBE functional. The data in green are calculated with the GGA-PBE functional and contain one hydrogen atom in the dimer pore structure. Notice how introducing a hydrogen atom drastically stabilise the (d) structure.*

6.8 Wagnerian/Non-Wagnerian oxidation

From the formalism developed in Paper V a thickness-dependent activation energy for diffusion is proposed. The effective diffusivity of oxygen vacancies of charge q, $D^q_{eff}(X)$, is given by

$$D^q_{eff}(X) = D^q_{bulk} \exp\left[-\frac{q^2 C^{q+}_{V_O}}{8\varepsilon\varepsilon_0 k_B T} X^2 \right] \tag{6.7}$$

where X is the oxide thickness, D^q_{bulk} is the diffusivity constant for vacancy of charge q in bulk, $C^q_{V_O}$ is the concentration of charged oxygen vacancies, ε is the relative permittivity, ε_0 is the vacuum permittivity, k_B is the Boltzmann constant, and T is the temperature. Given a constant concentration of charged oxygen vacancies, the activation energy increases for the formation of transient charged oxygen vacancies has a quadratic thickness dependence. From Eq. 6.7, a sub-parabolic oxide thickness curve is derived,

$$X = \left\{ \lambda_q^2 \ln\left(1 + \frac{2K^q_p}{\lambda_q^2} t \right) \right\}^{\frac{1}{2}} \tag{6.8}$$

where t is time, $\Delta\mu$ is the electro-chemical potential,

$$K^q_p = D^q_{bulk} \frac{\Delta\mu}{k_B T} \tag{6.9}$$

and

$$\lambda_q^2 = \frac{8\varepsilon\varepsilon_0}{q^2 C^{q+}_{V_O}} k_B T. \tag{6.10}$$

The total activation energy W for transport of oxygen vacancies by utilizing channels, which propagate electrons and charged vacancies separately, becomes

$$W = W^q_{bulk} + \frac{k_B T}{\lambda_q^2} X^2. \tag{6.11}$$

The first term in Eq. 6.11 represents the activation energy for bulk diffusion, while the second term is the thickness-dependent activation energy. It is associated with the forming of charged vacancies. This second term causes sub-parabolic oxide growth in classical Wagnerian oxidation theory with H_2 evolution. When W^q_{bulk} is large, the thickness-dependent term will not impact the scale

growth. If on the other hand W^q_{bulk} is small, then the sub-parabolic behavior will dominate the mass gain curve. Relevant here is that charged oxygen vacancies in t$-ZrO_2$ display $\sim$0.2 eV activation energies for diffusion, i.e., five times smaller than those for uncharged vacancies. Equation 6.11 says that for constant density of charged vacancies, the cost for the formation of additional charged vacancies increases with thickness of barrier oxide to the power of two. The hydrogen pick-up channel opens owing to the slowing down of the Wagnerian channel, which in turn precedes the transition to the next cycle. We propose that the charging of the oxide causes the build-up of V_O concentration close to the metal/oxide interface owing to the dissolution of oxygen into the alloy. A symptom of the oxide dissolution process is neutral oxygen vacancies accumulation, super-saturation, and possible hydrogen-assisted nucleation late in each cycle. The formation of pores was taken to offer easy paths for short-circuiting hydrogen transport through the oxide [9, 23], resulting in the avalanching hydrogen pick-up [24] reported to precede the breakdown of the barrier oxide, the latter resulting from increased loss of mechanical integrity of the barrier oxide.

6.9 Fate of hydrogen

To have an ongoing oxidation process of zirconium alloys with water as oxygen carrier, reduction of protons are needed. Ideally in zirconium cladding applications, the oxidation should be accompanied by hydrogen gas evolution but a fraction is absorbed in the alloy matrix that also is more energetically favorable than H_2, see Fig. 6.12. The impact of oxygen concentration on co-absorption of hydrogen in Zr is examined and found to be independent for oxygen-zirconium ratios up to 1:1. Protons is transported through the barrier oxide by concentration driven diffusion in form of hydroxides, as water will hydroxylate inner interfaces of e.g. grain boundaries and small cracks. Protons are reduced when they coincide with electrons and hydride ions can form.

Two channels are taken to jointly constitute the oxidation process. One according to classical oxidation theory involving hydrogen evolution when transport of electrons through the tetragonal phase is easy. Depending on concentration of protons, and concentration and type of transition metal in grain boundary, the hydride ion can recombine with a proton and form hydrogen gas. Hydrogen gas formed on e.g. iron sites in GB can be dissociated to hydride ion and proton again on nickel sites.

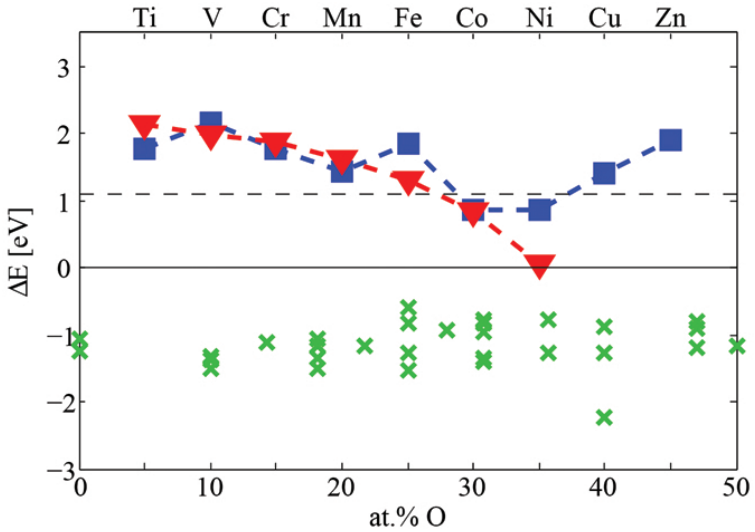

Figure 6.12: *Energetics for different compounds with 2H relative H_2 in gas phase (solid line at 0 eV). Dashed line at 1.1 eV corresponds to H_2 in grain boundary. Red triangles corresponds to proton and hydride ion associated with TM in oxidation state +III and blue squares to oxidation state +II, TM seen in top x-axis. Green cross represent 2H dissolved in zirconium structures with initial oxygen concentrations shown in bottom x-axis. Dissolved hydrogen in the zirocinium matrix are more stable than both hydrogen gas and the hydride ions.*

The second channel reflected by inwards transport of protons causing hydrogen pick-up opens when the transport of electrons becomes reduced due to oxide scale charging. Formation of charged oxygen vacancies are then suppressed and the concentration of neutral vacancies increases. The protons and electrons coincide closer to the oxide/metal interface due to the continued inwards diffusion of protons so that the location of the cathode is closer to the oxide/metal interface. In addition, hydride ions can nucleate coalescing of neutral oxygen vacancies and these can, if favorable oriented, constitute an easy transport of hydride ions through the oxide to the oxide/metal interface where neutral hydrogen is incorporated in the metal.

As seen in Fig. 6.12, dissolved hydrogen in the zirconium matrix are far more stable than both hydrogen gas and the hydride ions. Thermodynamically, hydrogen uptake is inevitable. The only way to prohibit it is to make sure that the hydrogen gas is formed before the hydrogen reach the zirconium matrix.

Chapter 7

Summary

In this thesis the mechanism for water induced corrosion of zirconium is studied using density functional theory. Anode and cathode reactions of the system are explored and a charge dependent oxygen vacancy transport through zirconia is identified. The aim of this study, as a part of the MUZIC-2 program, is to increase the knowledge about the mechanisms that govern hydrogen uptake in zirconium alloys. As the hydrogen uptake mechanisms are closely linked to the overall corrosion, the mechanisms controlling oxidation are needed in order to understand, predict and control hydrogen uptake.

A detailed mechanism for electro-catalytic hydrogen evolution is articulated, where the mechanism comprises formation of a transition metal associated hydride ion that recombine with a proton forming H_2. The cathode reaction is set to be the formation of the hydride ion. Electronic characterization of hydride ion and vibration frequency for some hydride ion species are presented. The vibration frequencies are found to be distinct from proton frequencies in hydroxide. A hydrogen evolution reaction from proton-hydride ion recombination is identified and correlation between energetics of proton-hydride ion recombination and hydrogen pickup fraction is found. Crucial for energetics of the hydrogen evolution reaction are change in coordination of transition metal ions upon release of H_2 into the grain boundary. The concept of confinement effect is introduced where the environment of the H_2 molecule affect the energy of the molecule in the grain boundary. The anode reaction is set to be the charging of oxygen vacancies that are formed as oxygen ions from the oxide are dissolved in the metal matrix. The oxygen dependence of the anode potential is examined along with the impact of

co-absorption of oxygen and hydrogen in the α-Zr matrix and is found to be independent for oxygen-zirconium ratios up to 1:1.

Two channels are taken to jointly constitute the oxidation process: one according to classical oxidation theory involving hydrogen evolution and the second reflected by inwards transport of protons causing hydrogen pick-up. Wagner theory and Tedmon kinetics are modified to include effects of oxide scale charging by arguing that activation energy for diffusion of charged oxygen vacancies also include the actual charging upon formation. Bulk activation energies for oxygen vacancy diffusion are calculated. Activation energies are dependent of the charge of the vacancy. Lower barriers are found in t$-ZrO_2$ compared to m$-ZrO_2$, especially for charged vacancies.

Hydrogen assisted build-up of nano-porosity is also addressed. The drive for nucleation of neutral oxygen vacancies is examined. Hydrogen is found to assist vacancy nucleation and a mechanism for hydrogen assisted build-up of nano-porosity is proposed. Activation barrier for hydrogen transfer between two V_O positions is calculated and conditions for hydrogen permeation through the barrier oxide by cooperating in pore formation is explored.

The direct and obvious industrial context where the research presented in this thesis is relevant is in the nuclear industry. As the research is of a fundamental nature, it may have much broader implications. Already, this research has influenced and inspired research in other industrial context, e.g. oxygen vacancy diffusivity in alumina formers [120, 121], interplay of water and reactive elements in oxidation of alumina-forming alloys [122], high temperature corrosion of stainless steels in low oxygen activity environments [123], magnesium alloy corrosion [124] and atmospheric corrosion of aluminum alloys [125].

Chapter 8

Future work

During this study, many interesting question have been answered but they have also raised many new questions. One of the major constrains of this study is that the effect of irradiation is not included, but in the nuclear application the effect of irradiation is crucial. Autoclave oxidation of zirconium is a good model system but there are differences compared to zirconium oxidation during neutron irradiation in a reactor. A suitable continuation of this study would be to examine the mechanistic reasons for the differences in oxidation and hydriding behavior between autoclave and in-reactor oxidation. This would include the impact of irradiation on

1. defect formations and their healing,
2. general thermodynamical materials aspects owing to the different time scales involved,
3. opening and closing of easy electron transport paths,
4. electron assisted proton transport paths,
5. oxygen dissolution in matrix contrasting that of autoclave,
6. oxygen vacancy V_O transport,
7. V_O related generic hydrogen assisted nano-porosity,
8. and the role of water chemistry in particular Li^+ on hydrogen uptake.

Other interesting tasks are to determine the impact of co-absorption of oxygen and alloying elements on the anode potential and make connection between DFT and thermodynamics exploring the potential of a novel cellular automata approach [126].

Chapter 9

List of abbreviations

APT Atom Probe Tomography

at.% Atomic procent, fraction of atoms not by weight.

BWR Boiling Water Reactor

CANDU Canadian deuterium-uranium, type of nuclear reactor

DFT Density Functional Theory

DSPP DFT Semi-core Pseudopotential

EBSD Electron BackScatter Diffraction

EELS Electron Energy Loss Spectroscopy

EPRI Electric Power Research Institute (US)

FIB Focused ion beam

GB Grain Boundary

GGA Generalized Gradient Approximation

HCP Hexagonal close-packed

HER Hydrogen Evolution Reaction

HPU Hydrogen Pick-Up

HPUF Hydrogen Pick-Up Fraction

HTCPM High-Temperature Corrosion and Protection of Materials

KS Kohn Sham

LDA Local Density Approximation

LOCA Loss Of Coolant Accident

LWR Light Water Reactor

m-ZrO_2 monoclinic zirconium dioxide

MUZIC Mechanistic Understanding of Zirconium Corrosion

PWR Pressurized Water Reactor

SPP Second Phase Particle

TM Transition Metal

t-ZrO_2 tetragonal zirconium dioxide

XRD X-ray Diffraction

zirconia Zirconium oxide

Zry Zircaloy

Bibliography

1. Amano, Y. Nuclear Power in the 21th century. *IAEA Bulletin* **54,** 2 (2013).
2. Stocker, T. F., Qin, D., Plattner, G.-K., Tignor, M. M., Allen, S. K., Boschung, J., Nauels, A., Xia, Y., Bex, V. & Midgley, P. M. *Climate Change 2013: The Physical Science Basis, Working Group I Contribution to the Fifth Assessment Report of the Intergovernmental Panel on Climate Change, Summary for Policymakers* tech. rep. (Intergovernmental Panel on Climate Change, IPCC, 2013).
3. Bychkov, A. Nuclear Power Today and Tomorrow. *IAEA Bulletin* **54,** 7 (2013).
4. Van der Zwaan, B. *Energy Strategy Reviews* **1,** 296–301 (2013).
5. Akashi, O., Hanaoka, T., Masui, T. & Kainuma, M. *Climatic Change* **123,** 611–622 (2014).
6. Riahi, K. *Global Energy Assessment - Toward a Sustainable Future,* 1203–1306 (2012).
7. IEA. *World Energy Outlook* (2012).
8. Tavoni, M. & van der Zwaan, B. *Environmental Modeling and Assessment* **16,** 431–440 (2011).
9. Vaillancourt, K., Labriet, M., Loulou, R. & Waaub, J. P. *Energy Policy* **36,** 2296–2307 (2008).
10. Lehtveer, M. & Hedenus, F. *Journal of Risk Research* **18,** 273–290 (2015).

11. Rickover, H. G., Geiger, L. D. & Lustman, B. *History of the development of zirconium alloys for use in nuclear reactors* tech. rep. (Division of Naval Reactors, 1975).
12. Thomas, D. E. in *Metallurgy of Zirconium* (eds Lustman, B. & Kerze, F.) chap. 11 (McGraw-Hill, New York, 1955).
13. Kass, S. *Journal of the Electrochemical Society* **107,** 594–497 (1960).
14. Klepfer, H. H. *Journal of Nuclear Materials* **9,** 77–84 (1963).
15. Hohenberg, P. & Kohn, W. *Physical Review B* **136,** B864–B871 (1964).
16. Kohn, W. & Sham, L. J. *Physical Review* **140,** A1133–A1138 (1965).
17. Choppin, G., Liljenzin, J.-O. & Rydberg, J. in *Radiochemistry and Nuclear Chemistry* 3ed edition (Butterworth-Heinemann, Woburn, 2002).
18. Franklin, D. G. & Adamson, R. B. *Journal of Nuclear Materials* **159,** 12–21 (1988).
19. Dictionary of Inorganic and Organometallic Compounds. *Zirconium* Dec. 2013. `http://dioc.chemnetbase.com/`.
20. CRC Handbook of Chemistry and Physics Online. *Properties of the Elements and Inorganic Compounds: The Elements* 94rd Edition. Dec. 2013. `http://www.hbcpnetbase.com/`.
21. Chroneos, A., Yildiz, B., Tarancon, A., Parfitt, D. & Kilner, J. *Energy and Environmental Science* **4,** 2774–2789 (2011).
22. Balaram, N., Reddy, M., Reddy, V. & Park, C. *Thin Solid Films* **619,** 231–238 (2016).
23. Cales, B. *Clinical Orthopaedics and Related Research* **379,** 94–112 (2000).
24. Lemaignan, C. & Motta, A. T. in *Materials Science and Technology - A Comprehensive Treatment, Volume 10B: Nuclear Materials Part II* (ed Frost, B. R. T.) 1–51 (VCH, New York, 1994).
25. Neutron scattering and absorption properties. in *CRC Handbook of Chemistry and Physics, 97th Edition (Internet Version 2017)* (ed Haynes, W. M.) (CRC Press/Taylor & Francis, Boca Raton, FL, 2017).
26. *Waterside Corrosion of Zirconium Alloys in Nuclear Power Plants* tech. rep. IAEA-TECDOC-996 (IAEA, Vienna, 1998).
27. Lemaignan, C. in *Comprehensive Nuclear Materials* 217–232 (Elsevier Ltd, 2012).

28. Abriata, J. P., Garcés, J. & Versaci, R. *Bulletin of Alloy Phase Diagrams* **7,** 116–124 (1986).
29. Douglass, D. L. *Metallurgy of Zirconium* tech. rep. (IAEA, Vienna, 1971).
30. Roy, C. & David, G. *Journal of Nuclear Materials* **37,** 71–81 (1970).
31. Barberis, P. *Journal of Nuclear Materials* **226,** 34–43 (1995).
32. Barberis, P., Merle-Mejean, T. & Quintard, P. *Journal of Nuclear Materials* **246,** 232–243 (1997).
33. Yilmazbayhan, A., Motta, A., Comstock, R. J., Sabol, G. P., Lai, B. & Cai, Z. *Journal of Nuclear Materials* **324,** 6–22 (2004).
34. Yilmazbayhan, A., Breval, E., Motta, A. T. & Comstock, R. J. *Journal of Nuclear Materials* **349,** 265–281 (2006).
35. Wei, J., Frankel, P., Polatidis, E., Blat, M., Ambard, A., Comstock, R. J., Hallstadius, L., Hudson, D., Smith, G. D. W., Grovenor, C. R. M., Klaus, M., Cottis, R., Lyon, S. & Preuss, M. *Acta Materialia* **61,** 4200–4214 (2013).
36. Cox, B. *Journal of Nuclear Materials* **336,** 331–368 (2005).
37. Ni, N., Hudson, D., Wei, J., Wang, P., Lozano-Perez, S., Smith, G. D. W., Sykes, J. M., Yardley, S. S., Moore, K. L., Lyon, S., Cottis, R., Preuss, M. & Grovenor, C. R. M. *Acta Materialia* **60,** 7132–7149 (2012).
38. De Gabory, B., Dong, Y., Motta, A. T. & Marquis, E. A. *Journal of Nuclear Materials* **462,** 304–309 (2015).
39. Puchala, B. & Van der Ven, A. *Physical Review B* **88,** 094108 (2013).
40. Nicholls, R. J., Ni, N., Lozano-Perez, S., London, A., McComb, D. W., Nellist, P. D., Grovenor, C. R. M., Pickard, C. J. & Yates, J. R. *Advanced Engineering Materials* **17,** 6–22 (2015).
41. Hu, J., Garner, A., Ni, N., Gholinia, A., Nicholls, R. J., Lozano-Perez, S., Frankel, P., Preuss, M. & Grovenor, C. R. M. *Micron* **60,** 7132–7149 (2015).
42. Abriata, J., Bolcich, J. & Arias, D. *Bulletin of Alloy Phase Diagrams* **4,** 147–154 (1983).
43. Garde, A. M., Pati, S. R., Krammen, M. A., Smith, G. P. & Endter, R. K. in *Zirconium in the Nuclear Industry: 10th International Symposium* (eds Garde, A. M. & Bradley, E. R.) 384–402 (ASTM, West Conshohocken, 2009).

44. Pecheur, D., Lefebvre, F., Motta, A. T., Lemaignan, C. & Wadier, J. F. *Journal of Nuclear Materials* **189,** 318–332 (1992).
45. Tejland, P., Thuvander, M., Andren, H. O., Ciurea, S., Andersson, T., Dahlback, M. & Hallstadius, L. *Journal of ASTM International* **8** (2011).
46. Tejland, P. & Andren, H. O. *Journal of Nuclear Materials* **430,** 64–71 (2012).
47. Kim, H.-G., Park, J.-Y. & Jeong, Y.-H. *Journal of Nuclear Materials* **345,** 1–10 (2005).
48. Proff, C., Abolhassani, S., Dadras, M. M. & Lemaignan, C. *Journal of Nuclear Materials* **404,** 97–108 (2010).
49. Proff, C., Abolhassani, S. & Lemaignan, C. *Journal of Nuclear Materials* **416,** 125–134 (2011).
50. Proff, C., Abolhassani, S. & Lemaignan, C. *Journal of Nuclear Materials* **432,** 222–238 (2013).
51. Tejland, P., Andren, H. O., Sundell, G., Thuvander, M., Josefsson, B., Hallstadius, L., Ivermark, M. & Dahlback, M. *Oxidation mechanism in zircaloy-2 - The effect of SPP size distribution* in *ASTM Special Technical Publication* **STP 1543** (2015), 373–403.
52. Sundell, G., Thuvander, M. & Andren, H. O. *Corrosion Science* **65,** 10–12 (2012).
53. Tupin, M., Pijolat, M., Valdivieso, F. & Soustelle, M. *Journal of Nuclear Materials* **342,** 108–118 (2005).
54. Smith, T. *Journal of the Electrochemical Society* **112,** 560–567 (1965).
55. Pilling, N. B. & Bedworth, R. E. *Journal of the Institute of Metals* **29,** 529–582 (1923).
56. Griggs, B., Maffei, H. P. & Shannon, D. W. *Journal of the Electrochemical Society* **109,** 665–668 (1962).
57. Bryner, J. S. *Journal of Nuclear Materials* **82,** 84–101 (1979).
58. Motta, A., Yilmazbayhan, A., Comstock, R., Partezana, J., Sabol, G., Lai, B., Cai, Z., Dequeldre, Ramasubramanian, M., Abolhassani, S., Kammenzind, B. & Cox, B. *ASTM Special Technical Publication* **1467 STP,** 205–232 (2005).
59. Cox, B. *Journal of Nuclear Materials* **29,** 50–66 (1969).
60. Bradhurst, D. & Heue, P. *Journal of Nuclear Materials* **37,** 35–47 (1970).

61. Cox, B. *Journal of Nuclear Materials* **27,** 1–11 (1968).

62. Ni, N., Lozano-Perez, S., Jenkins, M. L., English, C., Smith, G. D. W., Sykes, J. M. & Grovenor, C. R. M. *Scripta Materialia* **62,** 564–567 (2010).

63. Pétigny, N., Barberis, P., Lemaignan, C., Valot, C. & Lallemant, M. *Journal of Nuclear Materials* **280,** 318–330 (2000).

64. Béchade, J.-L., Brenner, R., Goudeau, P. & Gailhanou, M. *Materials Science Forum* **404-407,** 803–808 (2002).

65. Motta, A. *JOM* **63,** 59–63 (2011).

66. Harada, M. & Wakamatsu, R. *ASTM Special Technical Publication* **1505 STP,** 384–402 (2009).

67. Zuzek, E., Abriata, J., San-Martin, A. & Manchester, F. *Bulletin of Alloy Phase Diagrams* **11,** 385–395 (1990).

68. Simpson, C. J. & Ells, C. E. *Journal of Nuclear Materials* **52,** 289–295 (1974).

69. Couet, A., Motta, A. T., Comstock, R. J. & Paul, R. L. *Journal of Nuclear Materials* **425,** 211–217 (2012).

70. Couet, A., Motta, A. T. & Comstock, R. J. *Journal of Nuclear Materials* **451,** 1–13 (2014).

71. Elmoselhi, M. B., Warr, B. D. & McIntyre, S. in *Zirconium in the Nuclear Industry: 10th International Symposium* (eds Garde, A. M. & Bradley, E. R.) 62–78 (ASTM, Philadelphia, 1994).

72. Cox, B. & Wong, Y.-M. *Journal of Nuclear Materials* **270,** 134–146 (1999).

73. Ramasubramanian, N., Perovic, V. & Leger, M. *ASTM Special Technical Publication* **1354 STP,** 853–876 (2000).

74. Kakiuchi, K., Itagaki, N., Furuya, T., Miyazaki, A., Ishii, Y., Suzuki, S., Terai, T., Yamawaki, M., Barberis, P., Kapoor, K., Kim, Y., Motta, A., Cox, B., Hallstadius, L. & Ramasubramanian, N. *ASTM Special Technical Publication* **1467 STP,** 349–366 (2005).

75. Une, K., Sakamoto, K., Aomi, M., Matsunaga, J., Etoh, Y., Takagi, I., Miyamura, S., Kobayashi, T. & Ito, K. *ASTM Special Technical Publication* **1529 STP,** 401–430 (2011).

76. Bossis, P., Lelièvre, G., Barberis, P., Iltis, X. & Lefebvre, F. *ASTM Special Technical Publication* **1354 STP,** 918–945 (2000).

77. Hatano, Y., Sugisaki, M., Kitano, K. & Hayashi, M. *ASTM Special Technical Publication* **1354 STP,** 901–917 (2000).

78. Berry, W. E., Dale, A. W. & Earl, L. W. *Corrosion* **17,** 109t–117t (1961).

79. Parfenov, B. G., Gerasimov, V. V. & Venediktova, G. I. *Corrosion of Zirconium and Zirconium Alloys (Korroziya tsirkoniya i ego splavov)* 118–120 (Atomizdat, Moskva, 1967).

80. Cox, B. in *Advances in Corrosion Science and Technology* (eds Fontana, M. G. & Staehle, R. W.) 173–391 (Plenum, New York, 1976).

81. Takeda, K., Harada, M., Ishii, Y. & Miyazaki, A. *Journal of Nuclear Science and Technology* **43,** 984–990 (2006).

82. Broy, Y., Garzarolli, F., Seibold, A. & Van Swam, L. *ASTM Special Technical Publication* **1354 STP,** 609–622 (2000).

83. Schrödinger, E. *Annalen der Physik* **384,** 361–376 (1926).

84. Born, M. & Oppenheimer, R. *Annalen Der Physik* **389,** 457–484 (1927).

85. Hartree, D. R. *Proceedings of the Cambridge Philosophical Society* **24,** 89–110 (1928).

86. Hartree, D. R. *Proceedings of the Cambridge Philosophical Society* **24,** 111–132 (1928).

87. Fock, V. *Zeitschrift Fur Physik* **61,** 126–148 (1930).

88. Slater, J. *Physical Review* **35,** 210–211 (1930).

89. Slater, J. *Physical Review* **34,** 1293–1322 (1929).

90. Sham, L. & Kohn, W. *Physical Review* **145,** 561–567 (1966).

91. Vosko, S. J., Wilk, L. & Nusair, M. *Canadian Journal of Physics* **58,** 1200–1211 (1980).

92. Perdew, J. P. & Wang, Y. *Physical Review B* **45,** 13244–13249 (1992).

93. Perdew, J. P., Burke, K. & Ernzerhof, M. *Physical Review Letters* **77,** 3865–3868 (1996).

94. Becke, A. D. J. *The Journal of Chemical Physics* **88,** 2547–2553 (1988).

95. Lee, C., Yang, W. & Parr, R. G. *Physical Review B* **37,** 785–789 (1988).

96. Adamo, C. & Barony, V. *Journal of Chemical Physics* **110,** 6158–6170 (1998).

97. Becke, A. D. *Journal of Chemical Physics* **98,** 5648–5652 (1993).

98. Stephens, P. J., Devlin, F. J., Chabalowski, C. F. & Frisch, M. J. *Journal of Chemical Physics* **98,** 11623–11627 (1994).

99. Mori-Sánchez, P., Cohen, A. J. & Yang, W. *Journal of Chemical Physics* **125,** 201102 (2006).

100. Cremer, D. *Molecular Physics* **99,** 1899–1940 (2001).

101. Polo, V., Kraka, E. & Cremer, D. *Molecular Physics* **100,** 1771–1790 (2002).

102. Cohen, A., Mori-Sánchez, P. & Yang, W. *Science* **321,** 792–794 (2008).

103. Versluis, L. & Ziegler, T. *Journal of Chemical Physics* **88,** 322–328 (1988).

104. Andzelm, J., Wimmer, E. & Salahub, D. R. in *The Challenge of d- and f-Electrons: Theory and Computation* (eds Salahub, D. R. & Zerner, M. C.) ACS Symposium serie 394 (American Chemical Society, Washington DC, 1989).

105. Ashcroft, N. W. & Mermin, N. D. *Solid State Physics* (Saunders collage, Philadelphia, 1976).

106. Payne, M., Teter, M. P., Allan, D. C., Arias, T. A. & Joannopoulos, J. D. *Review of Modern Physics* **64,** 1045–1097 (1992).

107. Delley, B. *Journal of Chemical Physics* **92,** 508–517 (1990).

108. CRC Handbook of Chemistry and Physics Online. *Thermochemistry, Electrochemistry, and Solution Chemistry: Electrochemical Series* 94rd Edition. Dec. 2013. `http://www.hbcpnetbase.com/`.

109. Adamo, C. & Barone, V. *Journal of Chemical Physics* **110,** 6158–6170 (1999).

110. Delley, B. *Journal of Chemical Physics* **113,** 7756–7764 (2000).

111. Clark, S. J., Segall, M. D., Pickard, C. J., Hasnip, P. J., Probert, M. J., Refson, K. & Payne, M. C. *Zeitschrift Fur Kristallographie* **220,** 567–570 (2005).

112. Accelrys Inc. *Materials Studio 6.0* Simulation software.

113. Monkhorst, H. J. & Pack, J. D. *Physical Review B* **13,** 5188–5192 (1976).

114. Govind, N., Petersen, M., Fitzgerald, G., King-Smith, D. & Andzelm, J. *Computational Materials Science* **28,** 250–258 (2003).

115. Delley, B. *Physical Review B* **66,** 1551251–1551259 (2002).

116. Vanderbilt, D. *Physical Review B* **41,** 7892–7895 (1990).

117. Balog, M., Schieber, M., Michman, M. & Patai, S. *Thin Solid Films* **47,** 109–120 (1977).

118. Hamann, D. R., Schlüter, M. & Chiang, C. *Physical Review Letters* **43,** 1494–1497 (1979).

119. Garner, A., Gholinia, A., Frankel, P., Gass, M., Maclaren, I. & Preuss, M. *Acta Materialia* **80,** 159–171 (2014).

120. Babic, V., Geers, C., Lindgren, M., Jönsson, B., Johansson, L. G., Svensson, J. E. & Panas, I. *Effects on Oxygen Vacancy Diffusivity of Substitutional 3d Elements Doping in alpha-Alumina* in *9th International Symposium on High-Temperature Corrosion and Protection of Materials, Les Embiez, France* (2016).

121. Babic, V., Geers, C., Jönsson, B. & Panas, I. *Electrocatalysis* **8,** 565–576 (2017).

122. Mortazavi, N., Geers, C., Esmaily, M., Babic, V., Sattari, M., Lindgren, K., Malmberg, P., Jönsson, B., Halvarsson, M., Svensson, J., Panas, I. & Johansson, L. *Nature Materials* **17,** 610–617 (2017).

123. Hooshyar, H. *High Temperature Corrosion of Stainless Steels in Low Oxygen Activity Enviromnets* PhD thesis (Chalmers University of Technology, 2016).

124. Esmaily, M., Svensson, J., Fajardo, S., Birbilis, N., Frankel, G., Virtanen, S., Arrabal, R., Thomas, S. & Johansson, L. *Progress in Materials Science* **89,** 92–193 (2017).

125. Esmaily, M., Svensson, J. E. & Johansson, L. G. *Corrosion* **72,** 1587–1596 (2016).

126. Jahns, K., Landwehr, M., Wübbelmann, J. & Krupp, U. *Oxidation of Metals* **79,** 107–120 (2013).